Statistics in Medicine

WILEY

Statistics in Medicine

RESEARCH ARTICLE

A Graph-Theoretic Approach to Detection of Parkinsonian Freezing of Gait From Videos

Qi Liu[1] | Jie Bao[2] | Xu Zhang[3] | Chuan Shi[4] | Catherine Liu[5] | Rui Luo[1]

[1]Department of Systems Engineering, City University of Hong Kong, Hong Kong, China | [2]College of Electronic Information Engineering, Huaiyin Institute of Technology, Huaiyin, China | [3]School of Mathematical Sciences, South China Normal University, Guangzhou, China | [4]School of Data Science, The Chinese University of Hong Kong, Shenzhen, China | [5]Department of Data Science and Artificial Intelligence, The Hong Kong Polytechnic University, Hong Kong, China

Correspondence: Rui Luo (ruiluo@cityu.edu.hk)

Received: 1 May 2024 | **Revised:** 15 January 2025 | **Accepted:** 24 January 2025

Funding: This research was supported by the City University of Hong Kong (9610639), the Hong Kong Polytechnic University (ZZQ2), the Hong Kong SAR Government (GRF15301123), the National Natural Science Foundation of China (12301338), and the Chengdu Municipal Office of Philosophy and Social Science (2024BS013).

Keywords: change point detection | Fréchet statistics | freezing of gait | graph Laplacian | Parkinson's disease

ABSTRACT

Freezing of Gait (FOG) is a prevalent symptom in advanced Parkinson's Disease (PD), characterized by intermittent transitions between normal gait and freezing episodes. This study introduces a novel graph-theoretic approach to detect FOG from video data of PD patients. We construct a sequence of pose graphs that represent the spatial relations and temporal progression of a patient's posture over time. Each graph node corresponds to an estimated joint position, while the edges reflect the anatomical connections and their proximity. We propose a hypothesis testing procedure that deploys the Fréchet statistics to identify break points in time between regular gait and FOG episodes, where we model the central tendency and dispersion of the pose graphs in the presentation of graph Laplacian matrices by computing their Fréchet mean and variance. We implement binary segmentation and incremental computation in our algorithm for efficient calculation. The proposed framework is validated on two datasets, Kinect3D and AlphaPose, demonstrating its effectiveness in detecting FOG from video data. The proposed approach that extracts matrix features is distinct from the prevailing pixel-based deep learning methods. It provides a new perspective on feature extraction for FOG detection and potentially contributes to improved diagnosis and treatment of PD.

1 | Introduction

Parkinson's disease (PD) is a chronic neurodegenerative disorder that significantly impacts the quality of life of affected individuals [1]. Among the various motor abnormalities associated with PD, Freezing of Gait (FOG) stands out as a pervasive and debilitating manifestation. FOG is characterized by intermittent episodes of gait disruption, where patients experience a temporary inability to move forward despite their intention to do so. These episodes occur unpredictably and can be triggered by specific situations, such as initiating gait, turning, or navigating narrow spaces. The intermittent nature of FOG makes it challenging to detect and analyze using traditional clinical evaluation methods. Furthermore, traditional methods for FOG detection rely heavily on wearable sensors or manual observation [2], both of which have limitations in terms of convenience, accuracy, and scalability.

To address the limitations of conventional FOG detection methods, this study introduces a novel graph-theoretic approach to

Qi Liu and Jie Bao contributed equally to this work and share co-first authorship.

detect FOG from video data. It induces matrix-type features in contrast to pixel-based features in deep learning methods [3]. By leveraging the concept of the Fréchet mean and Fréchet variance [4], we propose a framework that transforms video frames into graph Laplacian matrices, representing human joint sequences as a graph-based structure. Nodes in the graph represent individual body joints, while edges depict the spatial connections between them. To ensure mathematical stability, we employ a Singular Value Decomposition (SVD)-based algorithm [5] to approximate the nearest symmetric positive definite (SPD) matrix from the original Laplacian matrix.

The SPD property is crucial as it allows for the creation of a metric space, particularly through the use of the Log-Euclidean metric [6], which is essential for calculating the Fréchet mean and variance. By establishing a metric space for graph Laplacian matrices, we derive closed-form formulas for the Fréchet mean and variance and incorporate them in a test statistic. This test statistic is then deployed to detect break points within the video sequence, effectively identifying the initiation and termination moments of FOG episodes. The integration of Fréchet statistical methods into the analysis of PD freezing gait contributes significantly to the accurate detection and quantification of FOG events. This novel approach holds the potential to inform disease management and treatment strategies, offering more effective diagnostic and therapeutic approaches for PD and other gait disorders. The proposed framework is validated on public datasets, demonstrating its feasibility and superiority compared to baseline models.

The rest of the paper is organized as follows: Section 2 provides a comprehensive review of the current research status on PD freezing gait, its detection techniques, graph-based distance metrics, and Fréchet analysis of graph Laplacians. Section 3 defines the research problems in both video processing and graph statistics, proposing the theoretical and algorithmic framework for graph preprocessing and FOG change point detection. Section 4 presents the experimental validation of the methodology using public datasets, comparing its performance with baseline models. Finally, Section 5 concludes the article, discussing the significance of the study, the implications of the experiments, and future application directions.

2 | Related Works

2.1 | Parkinsonism Freezing of Gait

PD is a neurodegenerative disorder that significantly impacts motor functions, with FOG being one of its most prominent symptoms, affecting approximately 80% of PD patients [1]. FOG is characterized by hesitation and reluctance during the initiation, turning, and termination of walking tasks, manifesting as shuffling steps, reduced stride length and width, decreased walking speed, bodily stiffness, and loss of normal arm swing motion. Additionally, PD patients exhibit diminished gait amplitude [7].

Studies have shown that in the pre-swing phase preceding FOG, activities of the tibialis anterior muscle and ankle joint initiate prematurely but significantly shorten during the actual swing phase, correlating with the gradual reduction in stride length and stable step frequency prior to freezing [8, 9]. Step frequency, which refers to the pace at which an individual walks, typically falls within the range of 90–110 steps per minute in normal walking patterns. However, in PD, the rhythm can escalate to 149 steps per minute [10].

PD gait is characterized by irregular increases in stride, including inconsistent and asymmetric steps. Measuring regularity and stability is crucial for distinguishing PD-related gait abnormalities from those caused by aging [11], indicating that FOG is a patterned and quantifiable process. Non-contact methods offer unparalleled advantages in detecting features directly from a distance without omitting many characteristics.

Various methods have been employed to elucidate the pathophysiological mechanisms of FOG. Traditional clinical subjective assessments, such as the Postural Instability/Gait Difficulty (PIGD) scale [12], Freezing of Gait Questionnaire (FOG-Q) [13], and Unified Parkinson's Disease Rating Scale (UPDRS) [14], fail to form effective patterns and capture subtle abnormalities in gait characteristics, unlike quantitative methods.

Wearable devices, including Inertial Measurement Units (IMUs) [15], shoe insole pressure sensors [2], and portable Electromyography (EMG) [16], support gait signal collection and can be further configured for disease monitoring and quantitative assessment through signal processing and analysis. IMUs, composed of accelerometers, gyroscopes, and magnetometers, measure the force, angular rate, and orientation of objects, facilitating time-domain and frequency-domain feature analysis of gait signals [17]. Furthermore, electroencephalography (EEG) brain waves in PD patients [18] have been used for analyzing with varying levels of FoG severity.

2.2 | Video-Based Detection Approaches for FOG

Recent advances in computer vision and human pose estimation have developed easy-to-use, affordable, and clinically relevant techniques for recognizing Parkinson's gait. Pose estimation identifies human joints in images or videos and has been effectively used in gait analysis. Initially, vision-based gait studies used Microsoft Kinect sensors for 3D joint analysis in Parkinson's patients, but the Kinect's limited range (0.5–4.5 m) restricted its application [19].

The combination of consumer-grade devices and advanced computer vision algorithms has significantly reduced the cost of gait analysis. Existing human pose estimation libraries, such as OpenPose, Detectron, and AlphaPose, have demonstrated their proficiency in extracting accurate 2D joint pixel coordinates from video recordings [20]. Previous research has explored the use of 2D joint trajectories to calculate domain-specific features for identifying Parkinson's gait and dyskinesia rating in color videos [3, 21, 22]. Several studies have employed the Microsoft Kinect camera and its SDK to generate 3D skeletal data. Nguyen [23] proposed a method to predict gait abnormality index by using the joint coordinates of 3D skeletons as input to an auto-encoder and distinguishing abnormal gait based on reconstruction error. Jun [24] proposed an auto-encoder based on a bidirectional recurrent neural network to extract features from 3D skeletal data for

abnormal gait recognition and evaluated the performance of the discriminant model using these features.

Tian [25] introduced a novel temporal convolutional neural network model to assess the severity of PD in gait videos by extracting participants' 3D body skeletons and estimating the MDS-UPDRS score. Li [22] extracted human joint sequences from videos recorded by PD patients and computed motion features using pose estimation methods. They then applied random forests for multi-class classification and evaluated clinical scores based on UPDRS and the Unified Dyskinesia Rating Scale (UDysRS) [26]. Sabo [3] proposed the use of a spatio-temporal graph convolutional network (ST-GCN) architecture and training program to predict clinical scores of Parkinson's gait from videos of dementia patients. Hu [27] proposed a graph convolutional neural network architecture that represents each video as a directed graph to detect PD freezing gait, demonstrating good performance with an AUC of 0.887 on a dataset of more than 100 videos collected from 45 patients during clinical evaluation.

The spatio-temporal graph convolutional network (ST-GCN) leverages the inherent graph structure of human skeletons to provide an effective mechanism for learning directly from joint trajectories. In the spatial domain, skeleton data can be represented graphically, while convolutional functions on the time axis can capture temporal features such as joint dynamics (frequency, velocity). The advantage of ST-GCN is that it eliminates the need for developing and computing engineered gait features based on joint trajectories, as it can learn directly from joint trajectories to utilize the most important aspects of gait patterns. ST-GCN has been effectively combined with human pose estimation libraries to score leg agility in Parkinson's disease [28].

2.3 | Distance Metric for Graph Sequences

In addition, another key step in solving the FOG's detection is to evaluate the distance between the graph sequences. The term "metric" refers to a metric space, which is a set of distances defined between elements in a space that extends beyond traditional Euclidean geometry. This is essential for analyzing data distribution and detecting change points.

In this article, the Frobenius norm is used as a method to measure the distance between two metrics. This is an indispensable part of calculating the Fréchet mean and variance of data objects within the metric space. The Fréchet mean serves as the center of the data distribution by being the point that minimizes the average distance to all other points in the space, thus providing a measure of central tendency. The Fréchet variance, on the other hand, measures the spread around this mean, quantifying the variability of the data points relative to the mean, similar to what variance does in traditional statistics. This approach focuses on comparing the Fréchet variance before and after a potential change point. It does not require parameter adjustments except when defining cutoff intervals where no change point is expected.

Using the Frobenius norm to quantitatively measure the difference between two matrices is particularly useful in the context of covariance matrices and change point detection. Reference [4] provides theoretical support for the effectiveness of using the Frobenius norm in change point detection, thereby ensuring the method's stability under various conditions. Furthermore, they offer theoretical guarantees for the consistency of tests under continuous alternatives, ensuring the method's reliability in detecting change points. The proposed method is also versatile across different metric spaces, demonstrating its applicability to various data environments.

In this article, the metric space referenced utilizes the Log-Euclidean metric from the Reference [29], which compares Euclidean, Riemannian, and Log-Euclidean. The Log-Euclidean metric was finally adopted.

For the Euclidean metric, while it is simple, it is insufficient for tensor computations. Noise and non-linear operations often result in non-positive eigenvalues in clinical data. Regularization methods focusing on tensor characteristics, such as eigenvectors, fail to utilize the complete information contained in the tensor, leading to incomplete solutions. The Euclidean average of tensors causes the "swelling effect," where the calculated mean has a larger determinant than the original tensors, which is physically unrealistic.

Regarding the Riemannian metric, within the affine-invariant statistical framework, it eliminates the swelling effect observed in the Euclidean metric by ensuring that symmetric matrices with negative eigenvalues are considered infinitely distant from any tensor. Despite being effective, the affine-invariant metric has high computational costs due to the complex operations involving matrix inversions and logarithms. Introducing the Log-Euclidean metric simplifies computations by transforming tensor operations into vector operations, enhancing efficiency while maintaining theoretical robustness.

For the Log-Euclidean metric, it is well-defined for the logarithms of tensors and corresponds to symmetric matrices, establishing a one-to-one relationship between symmetric matrices and tensors. This relationship allows direct computation of tensor logarithms through diagonalization and eigenvalue transformations. Matrix exponential operations similarly map symmetric matrices back to tensors.

The simplicity of the Log-Euclidean metric arises from the commutativity of logarithmic multiplication, preserving distance invariance under matrix inversion and logarithmic multiplication, thus ensuring the robustness of tensor computations. Although not achieving full affine invariance, it demonstrates similar invariance, yielding consistent results across different coordinate systems. The similarity-invariant Log-Euclidean metric enhances the reliability of tensor computations in various applications. Additionally, the Log-Euclidean metric is easier to compute and exhibits greater anisotropy and computational efficiency. Its similarity extends to various tensor operations, including regularization. Anisotropic regularization using the Riemannian metric effectively reduces noise while preserving essential structural details in tensor fields. The Log-Euclidean framework simplifies the regularization process by converting tensor computations into Log-Euclidean operations. Regularization experiments show that the Log-Euclidean method produces better results compared to Euclidean methods, effectively addressing challenges posed by noise in diffusion tensor imaging.

In this article, the Log-Euclidean metric allows the application of standard algebraic operations to tensors through logarithmic representation, providing a robust framework for tensor processing. By preserving the algebraic structure of vector spaces, the Log-Euclidean framework simplifies Riemannian statistics and analysis, improving the efficiency of tensor processing. In this context, the Frobenius norm and Fréchet mean provide a direct method for averaging tensors, in contrast to the iterative nature of the affine-invariant mean. Converting tensors into symmetric matrices or six-dimensional vectors allows the application of classical vector processing tools, simplifying computations. This underscores the importance of the Frobenius norm in the context of change point detection in the data sequences focused on in this paper, making it highly suitable for the task.

The proposed approach capitalizes on the structural information of graph Laplacian matrices and the intrinsic geometry of human skeleton data. It leverages spectral methods and the Log-Euclidean metric for a computationally efficient framework that captures essential structural changes. As a result, the paper presents a novel mathematical method for analyzing large graph sequences. This not only circumvents the computational issues of previous techniques but also offers new perspectives on the dynamics of FOG, providing a promising tool for monitoring PD progression.

3 | Methodology

In this section, we present the details of our approach for detecting FOG from video data. The proposed method consists of several key steps, which are outlined as follows.

- **Pose Estimation:** We employ a pose estimator to extract a pose sequence from the input video. The pose estimator identifies the locations of key body joints in each frame, providing a structured representation of the human skeleton over time.
- **Graph Construction:** We devise a novel way to construct pose graphs based on the obtained pose sequence. Each frame is represented as a graph, where nodes correspond to individual body joints and edges represent the spatial connections between them. This graph-based representation allows us to extract matrix features and capture the spatial geometry and temporal evolution of the human skeleton.
- **Hypothesis Testing:** We deploy a hypothesis testing framework for detecting FOG based on the obtained graphs. We construct a test statistic based on the Fréchet mean and variance of the graph Laplacians, which captures both the average behavior and the dispersion of the graphs in the sequence.

By combining the graph-based representation, the Log-Euclidean metric, and the hypothesis testing framework, our approach provides a principled and effective way to detect FOG in video data. The proposed method takes advantage of the inherent graph structure of the human skeleton and leverages the geometric properties of the graph Laplacians to identify changes in gait patterns. The introduction of the metric space and the use of the Fréchet mean and variance allow us to quantify the similarity between graphs and detect significant deviations from normal gait behavior. This approach offers a robust and interpretable way to analyze the temporal evolution of the human skeleton and identify FOG episodes. Figure 1 provides a visual representation of the proposed detection framework.

In the following subsections, we provide a detailed description of each component of our methodology, including the graph construction, Fréchet statistics definition, and change point detection algorithm. We also discuss the theoretical foundations and practical considerations of our approach, highlighting its advantages and potential limitations.

3.1 | Pose-Based Graph Sequence

Our proposed method for analyzing gait features and detecting potential changes in movement patterns consists of two main phases. The first phase involves obtaining sequential gait features from video data, while the second phase focuses on constructing a sequence of graphs to represent the structure of the joint coordinates. Let's delve into the details of each phase:

1. Phase 1: Obtaining Sequential Gait Features
   In this phase, we extract body joint coordinates from the video data using one of two approaches:
   AlphaPose: AlphaPose is a powerful tool for estimating human pose in images and videos. By applying AlphaPose to each frame of the video, we obtain the coordinates of various body joints, such as ankles, knees, hips, shoulders, elbows, and wrists. These coordinates provide a sequential representation of the gait features throughout the video.
   Kinect SDK: Alternatively, if the video data is captured using a Microsoft Kinect device, we can directly obtain the joint coordinates using the Kinect SDK. The Kinect SDK provides a set of APIs that allow us to access the depth and skeleton data from the Kinect sensor. By utilizing these APIs, we can extract the joint coordinates for each frame of the video, resulting in a sequential representation of the gait features.

2. Phase 2: Constructing a Sequence of Graphs
   In the second phase, we introduce a novel feature extraction approach to handle the pose data obtained from Phase 1. We construct a sequence of graphs to represent the structure of the joint coordinates. Each graph in the sequence corresponds to a specific frame of the video and captures the relationships between the body joints at that particular instant.
   For each frame of the video, create a graph where the nodes represent the body joints, and the edges represent the connections between the joints. This results in a sequence of skeleton graphs representing the graph structure of the joints over time. Denote the graph sequence as $G^{(1)}, G^{(2)}, \ldots$, where each snapshot $G^{(t)} = \left(V^{(t)}, E^{(t)}\right)$ represents an undirected weighted graph observed at discrete time t. All skeleton graphs share the same set of nodes, denoted as $V^{(1)} = V^{(2)} = \cdots = V$.
   For a skeleton graph sequence $G^{(t)}$ with $N = \left|V^{(t)}\right|$ nodes, the (i, j) entry of the $N \times N$ adjacency matrix $A^{(t)}$ represents the edge weight between joints i and j. The adjacency matrix captures the proximity of the connected joints. Each entry $A_{ij}^{(t)}$ in the adjacency matrix is calculated using the

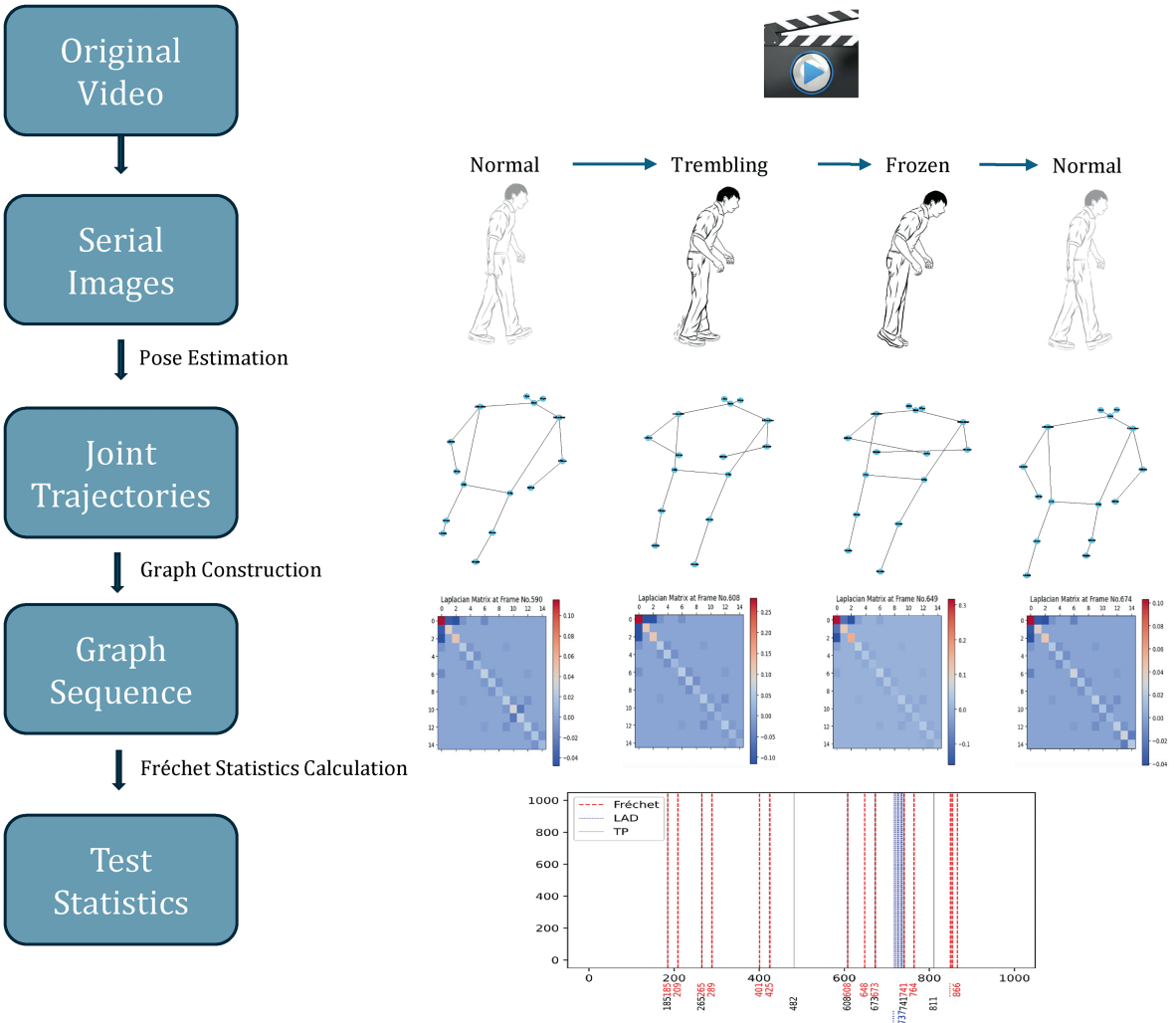

FIGURE 1 | Framework of the proposed graph-theoretic method for detecting FOG from video data. The method consists of three main steps: (1) pose estimation from video frames using AI-based pose estimation APIs such as AlphaPose, (2) construction of a sequence of pose graphs based on the estimated joint coordinates, where each graph represents the spatial relationships between body joints at a specific time point, and (3) calculation of test statistics using the Fréchet mean and variance of the graph Laplacian matrices. This novel approach effectively captures the temporal dynamics of gait patterns and enables the detection of potential FOG episodes by identifying significant deviations in the test statistics.

formula:

$$A_{ij}^{(t)} = \begin{cases} \frac{1}{\|\vec{w}_i - \vec{w}_j\|_2}, & \text{if joints } i \text{ and } j \text{ are connected by a bone} \\ 0, & \text{otherwise} \end{cases} \tag{1}$$

where $\vec{w}_i$ and $\vec{w}_j$ denote the coordinates of joints i and j, respectively, and $\|\cdot\|_2$ represents the Euclidean distance between the joint coordinates. By constructing this sequence of graphs, we capture the spatial relationships between the body joints and their evolution throughout the video. The adjacency matrices provide a compact representation of the gait features, taking into account the proximity of the connected joints. Based on the adjacency matrix, the graph Laplacian is defined as follows:

$$L_{ij}^{(t)} = \begin{cases} \sum_{k=1}^{N} A_{ik}^{(t)}, & \text{if } i = j \\ -A_{ij}^{(t)}, & \text{otherwise} \end{cases} \tag{2}$$

which uniquely determine the graph structure. The combination of these two phases, obtaining sequential gait features and constructing a sequence of graphs, forms the foundation of our proposed method. This approach allows us to effectively analyze the gait patterns and detect potential changes or anomalies in the movement data.

3.2 | FréChet Statistics of Graph Laplacians

To quantify the distance between two graphs, we introduce a metric space that enables us to measure the similarity between them based on their geometric properties. The Frobenius metric, defined as $\delta_F(X,Y) = \|X - Y\|_{\mathrm{F}} = \sqrt{\sum_{i=1}^{m}\sum_{j=1}^{n}(x_{ij} - y_{ij})^2}$, is a commonly used metric for matrices, but it suffers from the swelling effect, that is, the determinant of the average is larger than any of the original determinants [30]. To overcome this issue, we define the distance between two graphs as the Log-Euclidean metric of the nearest Symmetric Positive Definite

(SPD) matrices of their respective graph Laplacians. Moreover, this metric allows for a closed-form Fréchet mean, enabling us to characterize the average structure of a sequence of graphs.

The graph Laplacian $L^{(t)}$ is positive semi-definite, and its rank equals the number of nodes minus the number of communities, that is, disconnected components in the graph. Ginestet [31] characterize the set of $N \times N$ graph Laplacians with rank l as a submanifold of $\mathbb{R}^{N^2}$ of dimension $Nl - l(l+1)/2$.

The singularity of the graph Laplacian restricts the application of SPD metrics, such as the Log-Euclidean metric. To avoid this issue, we identify the nearest symmetric positive definite (SPD) matrix to $L^{(t)}$ in the Frobenius norm. This algorithm is based on the SVD of $L^{(t)}$ and is numerically stable and efficient. The resulting SPD, $\tilde{L}^{(t)}$, is then used in place of $L^{(t)}$ in defining the metric space. For directed graphs, Theorem 2 in the article [32] provides the 2-norm distance between a matrix (which may not be symmetric) and the nearest symmetric positive semidefinite (SPSD) matrix. We then use the algorithm [5] to identify the nearest SPD of the original graph Laplacian.

We define a metric space $(\tilde{\mathcal{L}}, \mathrm{d})$ for the graph snapshots. $\tilde{\mathcal{L}}$ is the set of the nearest SPD matrices of graph Laplacians, and d is a function $\mathrm{d} : \tilde{\mathcal{L}} \times \tilde{\mathcal{L}} \to \mathbb{R}_+$. We define d using the Log-Euclidean metric $\delta_{LE}(X, Y) = \|\log(X) - \log(Y)\|_{\mathrm{F}}$. The Log-Euclidean metric is defined as a bi-invariant metric on the Lie group [33] of SPD matrices, which is viewed as the classical Euclidean metric on the vector space [6]. Given i.i.d. random variables $\tilde{L}^{(1)}, \ldots, \tilde{L}^{(n)} \sim F$ in $(\tilde{\mathcal{L}}, \mathrm{d})$, the Fréchet mean has a unique closed-form solution [6]:

$$\mu_{\tilde{L}} = \exp(\mathbb{E}(\log(\tilde{L}))), \quad \overline{X}_{\tilde{L}} = \exp\left(\frac{1}{n}\sum_{i=1}^{n}\log\left(\tilde{L}^{(i)}\right)\right) \tag{3}$$

where $\mu_{\tilde{L}}$ and $\overline{X}_{\tilde{L}}$ are the population and sample Fréchet means, respectively. $\overline{X}_{\tilde{L}}$ is asymptotically consistent [34]. Besides, the population and sample Fréchet variances for $\tilde{L}^{(1)}, \ldots, \tilde{L}^{(n)} \sim F$ are:

$$\sigma^2_{\tilde{L}} = \mathbb{E}\left(\mathrm{d}^2\left(\mu_{\tilde{L}}, \tilde{L}\right)\right) \tag{4}$$

$$s^2_{\tilde{L}} = \frac{1}{n}\sum_{i=1}^{n}\mathrm{d}^2\left(\overline{X}_{\tilde{L}}, \tilde{L}^{(i)}\right) \tag{5}$$

$$= \frac{1}{n}\sum_{i=1}^{n}\left\|\frac{1}{n}\sum_{j=1}^{n}\log\left(\tilde{L}^{(j)}\right) - \log\left(\tilde{L}^{(i)}\right)\right\|^2_{\mathrm{F}} \tag{6}$$

3.3 | FréChet Statistics-Based FOG Detection

Having processed the video data into a sequence of graphs and defined a metric space for graph Laplacians, we now focus on the detection of FOG episodes. The key idea is to formulate the FOG detection problem as a graph change point detection task, where the goal is to identify significant changes in the statistical properties of the graph sequence over time.

To detect the change points, we leverage the geometric properties of the graph Laplacians in the metric space defined in Section 3.2. By comparing the Fréchet means and variances of the graph Laplacians across different segments of the sequence, we can identify significant deviations from the baseline gait behavior. Specifically, we employ a hypothesis testing framework to assess the statistical significance of the changes in the graph properties. We construct a test statistic based on the Fréchet mean and variance, which captures both the average behavior and the dispersion of the graphs within each segment. By sliding a window across the graph sequence and computing the test statistic for each window, we can identify the locations where the gait patterns undergo significant changes. These change points correspond to the transitions between normal gait and FOG episodes.

Let us consider an independent time-ordered sequence $\left\{Y^{(i)}\right\}_{i=1}^{n}$ that takes values in a metric space $(\tilde{\mathcal{L}}, \mathrm{d})$ defined in Section 3.1.2. In the simplest case, we hypothesize that there is at most one change point location, denoted by $0 < \tau < 1$. Specifically, $Y^{(1)}, \ldots, Y^{(\lfloor n\tau \rfloor)} \sim F_1$ and $Y^{(\lfloor n\tau \rfloor + 1)}, \ldots, Y^{(n)} \sim F_2$, where F_1 and F_2 are unknown probability measures on $(\tilde{\mathcal{L}}, \mathrm{d})$ and $\lfloor x \rfloor$ is the greatest integer less than or equal to x. In this context, the aim is to test the null hypothesis of distribution homogeneity, denoted by $H_0 : F_1 = F_2$, against the alternative hypothesis of a single change point, denoted by $H_1 : F_1 \neq F_2$.

To characterize the statistical properties of data from two segments separated by a potential change point $u \in \mathcal{I}_c = [c, 1-c] \subset [0, 1]$, we compute the sample Fréchet mean of the segment consisting of observations before and after $\lfloor nu \rfloor$ as

$$\overline{X}_{[0,u]} = \arg\min_{l \in \tilde{\mathcal{L}}} \frac{1}{\lfloor n\tau \rfloor}\sum_{i=1}^{\lfloor n\tau \rfloor}\mathrm{d}^2\left(Y^{(i)}, l\right) \tag{7}$$

$$\overline{X}_{[u,1]} = \arg\min_{l \in \tilde{\mathcal{L}}} \frac{1}{n - \lfloor n\tau \rfloor}\sum_{i=\lfloor n\tau \rfloor + 1}^{n}\mathrm{d}^2\left(Y^{(i)}, l\right) \tag{8}$$

and the corresponding sample Fréchet variance are:

$$s^2_{[0,u]} = \frac{1}{\lfloor n\tau \rfloor}\sum_{i=1}^{\lfloor n\tau \rfloor}\mathrm{d}^2\left(Y^{(i)}, \overline{X}_{[0,u]}\right) \tag{9}$$

$$s^2_{[u,1]} = \frac{1}{n - \lfloor n\tau \rfloor}\sum_{i=\lfloor n\tau \rfloor + 1}^{n}\mathrm{d}^2\left(Y^{(i)}, \overline{X}_{[u,1]}\right) \tag{10}$$

The contaminated version of Fréchet variances can be obtained by replacing the Fréchet mean of a segment with the mean of the complementary segment. This leads to the definitions:

$$\left(s^2_{[0,u]}\right)^C = \frac{1}{\lfloor n\tau \rfloor}\sum_{i=1}^{\lfloor n\tau \rfloor}\mathrm{d}^2\left(Y^{(i)}, \overline{X}_{[u,1]}\right) \tag{11}$$

$$\left(s^2_{[u,1]}\right)^C = \frac{1}{n - \lfloor n\tau \rfloor}\sum_{i=\lfloor n\tau \rfloor + 1}^{n}\mathrm{d}^2\left(Y^{(i)}, \overline{X}_{[0,u]}\right) \tag{12}$$

which are guaranteed to be at least as large as the correct version (4). The differences $\left(s^2_1\right)^C - s^2_{[0,u]}$ and $\left(s^2_2\right)^C - s^2_{[u,1]}$ can be interpreted as measures of the between-group variance of the two segments.

Suppose we fix some $u \in \mathcal{I}_c$. As a result of the central limit theorem for Fréchet variances [35], the statistic

$\sqrt{u(1-u)}(\sqrt{n}/\sigma)\left(s^2_{[0,u]} - s^2_{[u,1]}\right)$ has an asymptotic standard normal distribution under the null hypothesis H_0. Here, σ denotes the asymptotic variance of the empirical Fréchet variance. This result provides a powerful tool for statistical inference, allowing us to test hypotheses about differences in Fréchet variances between two segments of data. We adopt the following test statistic:

$$T_n(u) = \frac{u(1-u)}{\hat{\sigma}^2}\left[\left(s^2_{[0,u]} - s^2_{[u,1]}\right)^2 \right. \tag{13}$$

$$\left. + \left(\left(s^2_{[0,u]}\right)^C - s^2_{[0,u]} + \left(s^2_{[u,1]}\right)^C - s^2_{[u,1]}\right)^2\right] \tag{14}$$

The quantity $\left(s^2_{[0,u]} - s^2_{[u,1]}\right)^2$ provides a measure of the difference in Fréchet variances between two segments of data. Specifically, a larger value of $\left(s^2_{[0,u]} - s^2_{[u,1]}\right)^2$ indicates a greater difference in the variability of the data in the two segments. On the other hand, $\left(\left(s^2_{[0,u]}\right)^C - s^2_{[0,u]} + \left(s^2_{[u,1]}\right)^C - s^2_{[u,1]}\right)^2$ captures the difference in Fréchet means between the two segments.

Theorem 1 in [4] shows that under H_0, $\{nT_n(u) : u \in \mathcal{I}_c\}$ converges weakly[1] to the square of a standardized Brownian bridge on the interval $\mathcal{I}_c$, to perform a hypothesis test between H_0 and H_1, we use the statistic

$$\sup_{u\in\mathcal{I}_c} nT_n(u) = \max_{\lfloor nc\rfloor \le k \le n-\lfloor nc\rfloor} nT_n\left(\frac{k}{n}\right) \tag{15}$$

Here, $T_n(u)$ is a test statistic for the hypothesis test, which is computed for each potential change point $u \in \mathcal{I}_c$. To proceed, we obtain the $(1-\alpha)$ th quantile of $\sup_{u\in\mathcal{I}_c} \mathcal{G}^2(u)$, denoted as $q_{1-\alpha}$. Under H_0, we define the rejection region for a level α significance test as:

$$R_{n,\alpha} = \left\{\sup_{u\in\mathcal{I}_c} nT_n(u) > q_{1-\alpha}\right\} \tag{16}$$

Under H_1, which assumes a change point at $\hat{\tau} \in \mathcal{I}_c$, which maximizes the test statistic across all potential change points, we can locate it by finding the maximizer of the process $T_n(u)$:

$$\hat{\tau} = \arg\max_{u\in\mathcal{I}_c} T_n(u) = \arg\max_{\lfloor nc\rfloor \le k \le n-\lfloor nc\rfloor} T_n\left(\frac{k}{n}\right) \tag{17}$$

3.4 | Theory

In this section, we develop the theoretical foundation for our change-point detection methodology applied to the space of Symmetric Positive Definite (SPD) matrices endowed with the Log-Euclidean metric. We define the necessary estimators, establish key assumptions, and present the main consistency results that guarantee the reliability of our change-point estimation and hypothesis testing procedures.

For any $\alpha = \{\alpha_1, \alpha_2, \ldots, \alpha_n : 0 \le \alpha_i < 1, \sum_{i=1}^n \alpha_i = 1\}$, let

$$R_n(\omega, \alpha) = \sum_{i=1}^n \alpha_i \delta^2_{LE}(\tilde{L}_i, \omega) \quad \text{and} \quad \hat{\mu}_\alpha = \arg\min_{\omega\in\tilde{\mathcal{L}}} R_n(\omega, \alpha) \tag{18}$$

Furthermore, for any $0 \le \gamma \le 1$, let

$$S(\omega, \gamma) = \gamma E_1\left(\delta^2_{LE}(\tilde{L}, \omega)\right) + (1-\gamma)E_2\left(\sigma^2_{LE}(\tilde{L}, \omega)\right) \quad \text{and} \quad \mu_\gamma = \arg\min_{\omega\in\tilde{\mathcal{L}}} S(\omega, \gamma) \tag{19}$$

where:

- $\tilde{\mathcal{L}}$ denotes the space of SPD matrices nearest to graph Laplacians,
- δ_{LE} denotes the Log-Euclidean metric,
- $\tilde{L}_i$ represents the observed samples,
- ω, μ represent elements in the metric space $(\tilde{\mathcal{L}}, \delta_{LE})$.

We require the following assumptions, which are deemed to hold true regardless of whether the null hypothesis H_0 is established or not.

- **(A1)** For any $0 \le \gamma \le 1$, μ_γ exists and is unique. Additionally, there exists $\zeta > 0$ and $C > 0$ such that

$$\inf_{0\le\gamma\le1} \inf_{\delta_{LE}(\omega,\mu_\gamma)<\zeta} [S(\omega, \gamma) - S(\mu_\gamma, \gamma) - C\delta^2_{LE}(\omega, \mu_\gamma)] \ge 0 \tag{20}$$

  Note that this implies that under H_0,

$$\inf_{\delta_{LE}(\omega,\mu)<\zeta} \left\{E\left(\delta^2_{LE}(\tilde{L}, \omega)\right) - E\left(\delta^2_{LE}(\tilde{L}, \mu)\right) - C\delta^2_{LE}(\omega, \mu)\right\} \ge 0 \tag{21}$$

- **(A2)** For any $\alpha = \{\alpha_1, \alpha_2, \ldots, \alpha_n : 0 \le \alpha_i \le 1, \sum_{i=1}^n \alpha_i = 1\}$, $\hat{\mu}_\alpha$ exists and is unique almost surely. Additionally, for any $\varepsilon > 0$, there exists $\kappa_0 = \kappa_0(\varepsilon) > 0$ such that as $n \to \infty$,

$$P\left(\inf_{\alpha} \inf_{\delta_{LE}(\omega,\hat{\mu}_\alpha)>\varepsilon} [R_n(\omega, \alpha) - R_n(\hat{\mu}_\alpha, \alpha)] \ge \kappa_0\right) \to 1 \tag{22}$$

- **(A3)** Let $B_\delta(\omega) \subset \tilde{\mathcal{L}}$ be a ball of radius δ centered at ω, which is any arbitrary element in $\tilde{\mathcal{L}}$, and let $N(\varepsilon, B_\delta(\omega), \delta_{LE})$ be its covering number which is defined as the minimum number of balls of radius $\varepsilon > 0$ needed to cover $B_\delta(\omega)$ (see Section 2.1.1 of [37] for the definition and further details). Then, for any $\omega \in \tilde{\mathcal{L}}$,

$$\int_0^1 \sqrt{\log N(\varepsilon\delta, B_\delta(\omega), \delta_{LE})}d\varepsilon = O(1) \quad \text{as} \quad \delta \to 0 \tag{23}$$

The assumptions (A1)–(A3) are naturally satisfied in our setting for the following reasons:

1. The space of SPD matrices equipped with the Log-Euclidean metric is a Hadamard space (a complete, simply connected metric space with non-positive curvature) as established in Thanwerdas [38]. In Hadamard spaces, Fréchet means are unique provided they exist. The Log-Euclidean metric ensures convexity of the Fréchet functional, guaranteeing the existence and uniqueness of Fréchet means under mild regularity conditions on the distributions P_1 and P_2. Furthermore, the curvature conditions inherent to Hadamard spaces imply the quadratic lower bound required by (A1) with suitable constants ζ and C.

2. In Hadamard spaces, the Fréchet mean estimator $\hat{\mu}_\alpha$ is uniquely defined due to the convexity of the Fréchet functional and the uniqueness of the Fréchet mean. As the sample size increases, empirical Fréchet means converge uniformly to the population Fréchet mean, ensuring that $\hat{\mu}_\alpha$ consistently estimates μ_γ for appropriate γ. The consistent minimization of the Fréchet functional under the Log-Euclidean metric satisfies the second part of (A2), ensuring that deviations beyond ε incur a positive penalty bounded below by $\kappa_0(\varepsilon)$ [39, 40].

3. The space of SPD matrices with bounded entries under the Log-Euclidean metric exhibits polynomial metric entropy. Specifically:
   - The Log-Euclidean metric transforms the SPD matrix space into a Euclidean space via the matrix logarithm. Thus, the covering number $N(\varepsilon, B_\delta(\omega), \delta_{LE})$ behaves similarly to that of a standard Euclidean space of comparable dimension [37, 41].
   - For fixed dimensions, the covering number grows polynomially with respect to ε^{-1}. Hence, we can select $\beta = 1/\gamma$ for appropriate $\gamma > 0$ to satisfy the entropy condition in (A3), ensuring

$$\log N(\varepsilon, \tilde{\mathcal{L}}, \delta_{LE}) \leq \frac{K}{\varepsilon^\beta} \tag{24}$$

   for some constant $K > 0$.

These geometric and topological properties of the Log-Euclidean metric space of SPD matrices naturally lead to the satisfaction of our technical assumptions, providing a robust theoretical foundation for our statistical framework.

Theorem 1. (**Consistency of Change-Point Estimation**). *Under the alternative hypothesis H_1 and assumptions (A1)–(A3), the estimated change-point $\hat{\tau}$ satisfies*

$$\sup_{u \in \mathcal{I}_c} |T_n(u) - T(u)| = o_P(1) \quad \text{and} \quad |\hat{\tau} - \tau| = o_P(1) \quad \text{as} \quad n \to \infty$$

The above theorem establishes that our change-point estimator $\hat{\tau}$ converges in probability to the true change-point τ as the sample size n grows to infinity. Specifically, the supremum of the difference between the empirical test statistic $T_n(u)$ and its population counterpart $T(u)$ uniformly over the interval $\mathcal{I}_c$ becomes negligible. Consequently, the estimated change-point accurately identifies the location of the true change-point with increasing probability, ensuring the reliability of our estimation procedure under the alternative hypothesis.

Theorem 2. (**Consistency of the Test**). *Under H_1 and assumptions (A1)–(A3), for contiguous alternatives where*

$$\delta_{LE}(\mu_1, \mu_2) = a_n \quad \text{and} \quad |\sigma_1^2 - \sigma_2^2| = b_n$$

with $a_n, b_n \to 0$ as $n \to \infty$, the test power satisfies $\psi_n \to 1$, provided either $\sqrt{n}a_n \to \infty$ or $\sqrt{n}b_n \to \infty$.

This theorem ensures that our hypothesis test is consistent against contiguous alternatives. As the sample size increases, even subtle differences between the mean SPD matrices (μ_1 and μ_2) measured by the Log-Euclidean metric, or in their variability (σ_1^2 and σ_2^2), will be detectable with probability approaching one. In other words, the test becomes increasingly powerful, effectively rejecting the null hypothesis of no change-point when such a change exists, provided that the deviations in means or variances are sufficiently large relative to the sample size.

The satisfaction of Theorems 1 and 2 ensures that the test statistics of our algorithm are sufficiently significant to reject the null hypothesis of no change points. The proofs related to these theorems are provided in the appendix.

3.5 | Algorithm and Computing Complexity

By leveraging the closed form of the Fréchet mean (1) and variance (2), we have developed a recursive formula for updating these values incrementally, which is shown in the `IncrementalFréchetStatistics` function of Algorithm 1. This approach significantly reduces the time complexity from $\mathcal{O}(n^2)$ to $\mathcal{O}(n)$, making it computationally efficient while still maintaining accuracy.

To determine the number of change points, we employ a binary segmentation algorithm, which recursively partitions the graph sequence into smaller segments based on the test statistic. The algorithm identifies the most significant change points and continues to split the segments until a stopping criterion is met, such as a predefined threshold or a desired level of granularity. We present the proposed binary segmentation procedure that extends the proposed statistic $T_n(u)$ (9) to the multiple change point scenario. Binary segmentation is a computationally efficient tool that searches for multiple breakpoints in a recursive manner [42].

We present the procedure in the `BinarySegmentation` function in Algorithm 1. Furthermore, we have extended the point estimation of the algorithm to a confidence window by setting the window size. We will calculate the statistics near the point and identify all points within the window size that are greater than q1-alpha. For details, please refer to Algorithm 2.

1. Complexity Analysis
   The algorithm for calculating the nearest positive definite matrix consists of iterative projections onto subspaces, achieving linear convergence at best [5]. Each projection involves $\mathcal{O}(N^3)$ complexity due to the need to solve linear systems and perform spectral decomposition. Calculating the Fréchet mean within the Log-Euclidean metric necessitates computing the matrix exponential for each matrix, which has a time complexity of $\mathcal{O}(N^3)$. Thus, the time complexity for preprocessing each network snapshot is $\mathcal{O}(N^3 \log(1/E))$, where E represents the target error value. Algorithm 1 employs an incremental approach to calculate both the Fréchet statistics and their contaminated variants, with a time complexity of $\mathcal{O}(nN^2)$, where N^2 corresponds to the time complexity of computing the Frobenius inner product. Therefore the overall time complexity of Algorithm 1 is $\mathcal{O}(nN^3 \log(1/E))$.

ALGORITHM 1 | Multiple FOG change point estimation based on Fréchet statistics.

Input: Video, significance level α, minimum segment length parameter c, bootstrap sample size B, length of each bootstrap sample m.
Output: A set of detected change points $\hat{\mathrm{T}} = \{\hat{\tau}_1, \hat{\tau}_2, \dots\}$.

Transform the input video into a series of network snapshots $G^{(1)}, G^{(2)}, \dots, G^{(n)}$ that represent the skeleton frames detected by pose estimation tools like AlphaPose.
Calculate the sequence of nearest symmetric positive definite (SPD) matrices $\tilde{\mathrm{L}} = [\tilde{L}^{(1)}, \dots, \tilde{L}^{(n)}]$ using the algorithm in [5].
Output the estimated change points $\hat{\tau}_1, \hat{\tau}_2, \dots$ = BINARYSEGMENTATION($\tilde{\mathrm{L}}$).
function INCREMENTALFRECHETSTATISTICS($\tilde{\mathrm{L}}$)
    $\overline{X}_{[0,\frac{1}{n}]} = \tilde{L}^{(1)}$, $\overline{X}_{[\frac{n-1}{n},1]} = \tilde{L}^{(n)}$, $s^2_{[0,\frac{1}{n}]} = s^2_{[\frac{n-1}{n},1]} = 0$.
    for $t = 2, \dots, n$ **do** To reduce the accumulation of numerical errors of $\overline{X}_{[\cdot,1]}$ and $s^2_{[\cdot,1]}$, we compute their values in reverse order, starting from the last index and working backwards.
        $\overline{X}_{[0,\frac{t}{n}]} = \frac{t-1}{t}\overline{X}_{[0,\frac{t-1}{n}]} + \frac{1}{t}\tilde{L}^{(t)}$,
        $s^2_{[0,\frac{t}{n}]} = \frac{t-1}{t}s^2_{[0,\frac{t-1}{n}]} + \frac{1}{t}(\tilde{L}^{(t)} - \overline{X}_{[0,\frac{t-1}{n}]}) : (\tilde{L}^{(t)} - \overline{X}_{[0,\frac{t}{n}]})$, (: denotes the Frobenius product.)
        $\overline{X}_{[\frac{n-t}{n},1]} = \frac{t-1}{t}\overline{X}_{[\frac{n-t+1}{n},1]} + \frac{1}{t}\tilde{L}^{(n-t+1)}$,
        $s^2_{[\frac{n-t}{n},1]} = \frac{t-1}{t}s^2_{[\frac{n-t}{n},1]} + \frac{1}{t}(\tilde{L}^{(n-t+1)} - \overline{X}_{[\frac{n-t+1}{n},1]}) : (\tilde{L}^{(n-t+1)} - \overline{X}_{[\frac{n-t}{n},1]})$
    end for
    for $t = 1, \dots, n$ **do**
        $\left(s^2_{[0,\frac{t}{n}]}\right)^C = s^2_{[0,\frac{t}{n}]} + (\overline{X}_{[\frac{t}{n},1]} - \overline{X}_{[0,\frac{t}{n}]}) : (\overline{X}_{[\frac{t}{n},1]} - \overline{X}_{[0,\frac{t}{n}]})$,
        $\left(s^2_{[\frac{n-t}{n},1]}\right)^C = s^2_{[\frac{n-t}{n},1]} + (\overline{X}_{[\frac{t}{n},1]} - \overline{X}_{[0,\frac{t}{n}]}) : (\overline{X}_{[\frac{t}{n},1]} - \overline{X}_{[0,\frac{t}{n}]})$
    end for
    Compute $\{nT_n(\frac{t}{n})\}_{t=1,\dots,n}$ according to (15).
    return $\sup_{u\in\mathcal{I}_c} nT_n(u)$, $\arg\max_{u\in\mathcal{I}_c} T_n(u)$
end function
function BINARYSEGMENTATION($\tilde{\mathrm{L}}$)
    $q_{1-\alpha}$ =BOOTSTRAP(B, m, α) We refer the reader to Section 3.3 of the article [4] for the bootstrap scheme.
    $z, \hat{\tau}$ = INCREMENTALFRECHETSTATISTICS($\tilde{\mathrm{L}}$)
    if $z > q_{1-\alpha}$ **then**
        Update $\hat{\mathrm{T}} \leftarrow \hat{\mathrm{T}} \cup \{\hat{\tau}\}$
        BINARYSEGMENTATION($\tilde{L}^{(1)}, \dots, \tilde{L}^{(\lfloor n\hat{\tau}\rfloor)}$)
        BINARYSEGMENTATION($\tilde{L}^{(\lfloor n\hat{\tau}\rfloor+1)}, \dots, \tilde{L}^{(n)}$)
    end if
    return $\hat{\mathrm{T}}$
end function

4 | Empirical Evaluation

We evaluated the algorithm's performance, and the results are fully reproducible, and the codeanddataset for the experiments are publicly available.

4.1 | Baseline Method

Laplacian Anomaly Detection (LAD) [43] employs graph Laplacian spectra for detecting changes in a graph sequence. It begins with SVD computation of the Laplacian graph to obtain a low-dimensional representation, which captures the global view of graph snapshots and their connection to graph connectivity and low-rank approximation. This enables LAD to detect various graph changes in dynamic graphs, such as community structures and average edge weights, which may occur abruptly at any given time step [44]. These abrupt changes can be identified through short-term sliding windows [45]. LAD explicitly captures both short-term and long-term temporal relationships to simulate sudden and gradual changes in dynamic networks. However, time points that emit signals of graph pattern changes over an extended period may also carry significant importance [46]. In particular, underlying graph generation models may evolve. To effectively detect these change points, models need to infer graph behaviors beyond just the latest behavior. LAD is capable of modeling both short-term and long-term perspectives and explicitly comparing graph structures with typical behaviors [43].

Therefore, we use the LAD method as our benchmark, which starts by creating low-dimensional embeddings using the singular vectors from the graph Laplacian for the entire sequence. It then gathers these vectors over two distinct sliding window sizes to grasp the temporal dependencies. LAD determines z-scores through a comparison of the current embedding with past ones to pinpoint potential shifts. In contrast, our algorithm identifies changes within the Laplacian by measuring the Fréchet distance between recent graph Laplacian matrices. Our approach is more closely aligned with the network's inherent structure, potentially enhancing the detection of topological changes.

ALGORITHM 2 | A Confidence Window.

function BINARYSEGMENTATION-CW($\tilde{\mathrm{L}}$)
  $q_{1-\alpha}$ =BOOTSTRAP(B, m, α)[3]
  $z, \hat{\tau}$ = INCREMENTALFRECHETSTATISTICS($\tilde{\mathrm{L}}$)
  if $z > q_{1-\alpha}$ **then**
    Update $\hat{\mathrm{T}} \leftarrow \hat{\mathrm{T}} \cup \{\hat{\tau}\}$
    Given a confidence window size w.
    $\left[z_1, z_{1+w}\right], \left[\hat{\tau_1}, \hat{\tau_{1+w}}\right]$ = INCREMENTALFRECHETSTATISTICS $\left(\left[\tilde{L}^{(\lfloor n\hat{\tau}-\frac{w}{2}\rfloor)}, \tilde{L}^{(\lfloor n\hat{\tau}+\frac{w}{2}\rfloor)}\right]\right)$
    Calculate whether the interval $\left[z_1, z_{1+w}\right]$ is greater than $q_{1-\alpha}$
    Return to the confidence window $\left[\hat{\tau_{k_1}}, \hat{\tau_{k_2}}\right]$
    BINARYSEGMENTATION($\tilde{L}^{(1)}, \ldots, \tilde{L}^{(\lfloor n\hat{\tau}-\frac{w}{2}+k_1\rfloor)}$)
    BINARYSEGMENTATION($\tilde{L}^{(\lfloor n\hat{\tau}\rfloor+\frac{3w}{2}-k_2)}, \ldots, \tilde{L}^{(n)}$)
  end if
  return $\left[\hat{\tau_{k_1}}, \hat{\tau_{k_2}}\right]$
end function

In addition, we employed another statistic as a baseline method, which is also derived from the changes in Frechet mean and variance. We named it Frechet-SN [47]. This method is a change-point detection technique based on Self-Normalization (SN) and is suitable for time series data in non-Euclidean spaces.

4.2 | Datasets

We use natural gait videos collected from Toronto Rehabilitation Institute University Health Network (UHN), where the natural walking bouts of participating patients were recorded [3]. The datasets are sourced from anopen-sourcerepository. In the utilized dataset, the authors did not provide pose tracking or data preparation functions. Instead, they extracted gait information from individuals with Parkinson's disease using the AlphaPose library and the Microsoft Kinect library, tracking 2D or 3D skeletal trajectories under different gaits. Since these libraries independently predict joint positions for each frame of the input video, the authors performed additional processing to temporally connect and smooth the trajectories of the target individuals. The joint trajectories are centered at [100, 100, 100]. Therefore, this study employs the Kinect3D and AlphaPose sample datasets used by the aforementioned authors for demonstration purposes, specifically for detecting freezing gait changes.

Kinect 3D and AlphaPose are two distinct technologies utilized in different application domains, yet both are relevant to human body pose [3]. Kinect 3D is a depth sensor technology developed by Microsoft, which captures three-dimensional depth data of the surrounding environment through a combination of infrared and RGB cameras, along with infrared emitters and receivers. Meanwhile, AlphaPose is a deep learning-based human pose estimation system, akin to OpenPose. It operates on input data in the form of images or videos, utilizing techniques such as convolutional neural networks for pose estimation, with the output comprising coordinates for key body joints and pose information. In this study, we utilized AMBIENT, a ceiling-mounted Microsoft Kinect v2 system (1080 × 1920 pixels, 30 Hz). The Kinect 3D data is sourced from the Kinect v2 system depth sensor and Kinect Software Development Kit (SDK), wherein 3D skeletal trajectories are directly derived from its depth information. Conversely, the AlphaPose data is obtained from standard color videos recorded simultaneously with the capture of depth information using the Kinect v2 system. The 3D skeletal data and standard color videos are separately processed to extract joint trajectories and gait features. The Kinect 3D skeletal data and AlphaPose skeletal data used in this study are sourced from different patients, thus there is no need to worry about data source duplication.

4.2.1 | Kinect3d Dataset

The Kinect SDK [48, 49] device directly provides 3D joint trajectory data from the images. Sixteen spatiotemporal, variability, symmetry, and mechanical stability features of gait were calculated directly from the 3D joint trajectories. These gait features are described and validated [50, 51]. It is notable that the 3D joint positions extracted from Kinect are provided in meters, allowing distance measurements to be correlated with real-world units.

In the Kinect3D sample data, four files are provided, with three originating from the same ID and the fourth from a different ID that was abandoned. The three original datasets consist of normal gait data A and two freezing gait datasets B, C separated from each other. To detect change points, these three datasets need to be concatenated. Considering that datasets A, B, and C contain 127, 50, and 151 sequences, respectively, simple concatenation would result in too few change points, making it difficult to demonstrate the superiority of the algorithm. Therefore, the datasets A, B, and C are split into 3, 2, and 3 segments, respectively. The eight segmented datasets are labeled as a to h: a, b, c from normal gait A; d, e from freezing gait B; f, g, h from freezing gait C. The eight segments are interleaved and concatenated in the order a, d, b, f, e, g, c, h, with a counting range of [0, 327], totaling 328 image sequences. The seven concatenation points are located at "25", "43", "87", "117", "149", "242" and "300".

In Kinect3D, irrelevant data such as "x_min", "y_min", "z_min", "x_max", "y_max" and "z_max" are removed, retaining only the 25 nodes: "Head", "c7", "SpineShoulder", "Spine", "LShoulder", "LElbow", "LWrist", "LHand", "LHandTip", "LThumb", "RShoulder", "RElbow", "RWrist", "RHand", "RHandTip", "RThumb", "Sacr", "LHip", "LKnee", "LAnkle", "LFoot", "RHip", "RKnee", "Rankle", "RFoot". As shown in Figure 2, it presents a directed and weighted dynamic graph, where each node corresponds to a crucial skeletal joint of the human body, and each edge connects according to the normal human skeletal structure. Edge weights reflect the natural distance between skeletal joints in the camera, represented as the reciprocal of the Euclidean distance. The dataset is divided at a rate of 30 frames per second, with a total duration of 29.1333 s. In the analysis, every 0.0333 s is considered a separate time point, corresponding to the aforementioned image counting range of [0, 327], comprising 328 sequences of human skeletal graphs.

4.2.2 | Alphapose Dataset

The timing of footsteps is automatically identified by distinguishing the vertical position of the ankle key points and indicating

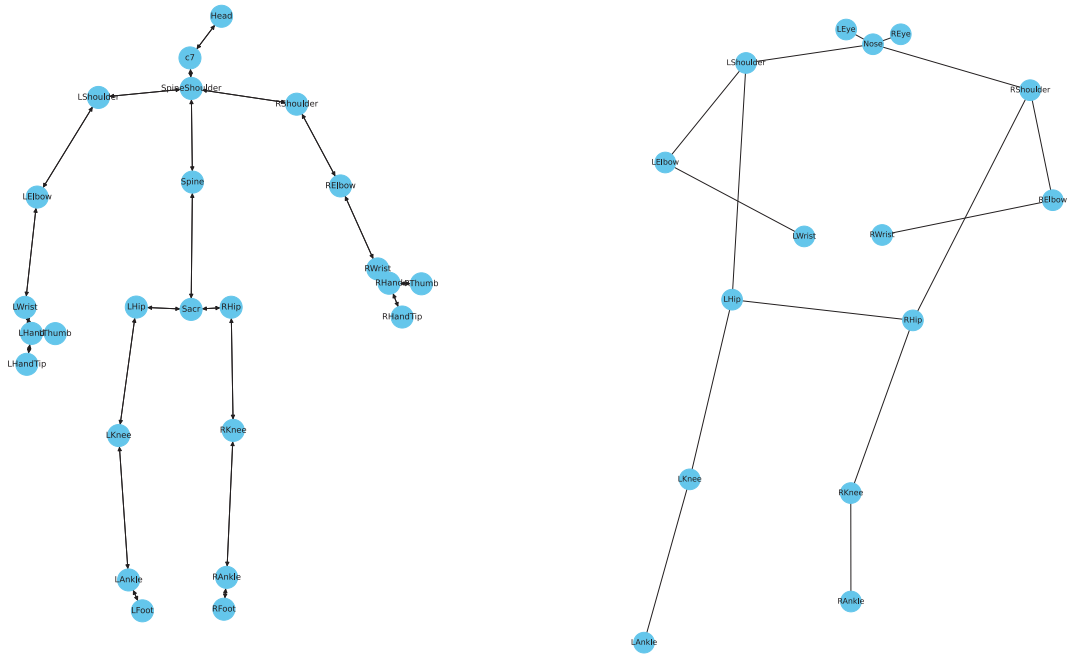

(a) **(b)**

FIGURE 2 | (a) Sequence at "125" in the Kinect3D dataset. (b) Sequence at "638" in the AlphaPose dataset.

the heel strike at 35% of each gait cycle peak [52]. Once the heel strike is identified, seven spatiotemporal and mechanical stability features of the gait are calculated, including step count, step frequency, average step width, average stability margin, the coefficient of variation of time, and the average index of step time. Ng et al. [53] provide a complete description of the method for detecting heel strikes and calculating these 2D gait features. Finally, using the detected footstep timings, the portion between the first step and the last step of each walk is extracted to ensure participants are walking continuously in the final joint trajectory. For each pose estimation library, this joint trajectory and gait feature extraction process is independently repeated, producing the AlphaPose feature set.

In the AlphaPose sample dataset, four files are provided, all originating from the same ID number and thus all being adopted for use. According to the author's annotations in these four original datasets, it is understood that there are two sets of normal gait data labeled A and B, and two sets of freezing gait data labeled C and D, each separated. As mentioned above, to prevent significant errors due to insufficient data sources and too few change points, we cannot simply concatenate these three sets of data. Therefore, in this study, each of the four datasets is separately trimmed into two segments. The eight segmented datasets are labeled as a to h: a, b from normal gait A; c, d from normal gait B; e, f from freezing gait C; g, h from freezing gait D. The eight segments are interleaved and concatenated in the order a, e, b, c, g, d, f, h, with a counting range of [0, 874], and the seven concatenation points are located at "185", "265", "482", "608", "673", "741", and "811".

It's important to note that, for the validation of the Precision of this algorithm, segments bc (at "482") represent normal gait, and segments fh (at "811") represent freezing gait. These specific segments should not be identified as change points, as they correspond to the same gait type at different time points. All other segments, excluding these two, involve the concatenation of freezing and normal gaits and should be identified as change points.

In AlphaPose, erroneous data "LEar" and "REar" (left and right ears) were removed, and irrelevant data "x_min", "y_min", "x_max", and "y_max" were eliminated. Only the following 15 nodes were retained: "Nose", "LEye", "REye", "LShoulder", "LElbow", "LWrist", "RShoulder", "RElbow", "RWrist", "LHip", "LKnee", "LAnkle", "RHip", "RKnee", "RAnkle". As shown in Figure 2, it presents a directed and weighted dynamic graph where each node corresponds to crucial skeletal joints of the human body, and each edge connects according to the normal human skeletal structure. Edge weights reflect the natural distance between skeletal joints in the camera, represented as the reciprocal of the Euclidean distance. The dataset is divided at a rate of 30 frames per second, with a total duration of 29.1333 s. In the analysis, every 0.0333 s is considered a separate time point, corresponding to the previously mentioned image counting range of [0, 874], comprising 875 sequences of human skeletal graphs.

4.3 | Experimental Results and Analysis

We define true positives (TP), false negatives (FN), true negatives (TN), and false positives (FP) between the actual time breakpoints and the ones identified by the algorithm. Based on these metrics, we compute the Precision, Recall, and F1-Score for evaluating the performance of the detection algorithms.

1. Kinect3D
   For Kinect3D, the results of detected multiple break points in time are displayed in Figure 3. It can be observed that

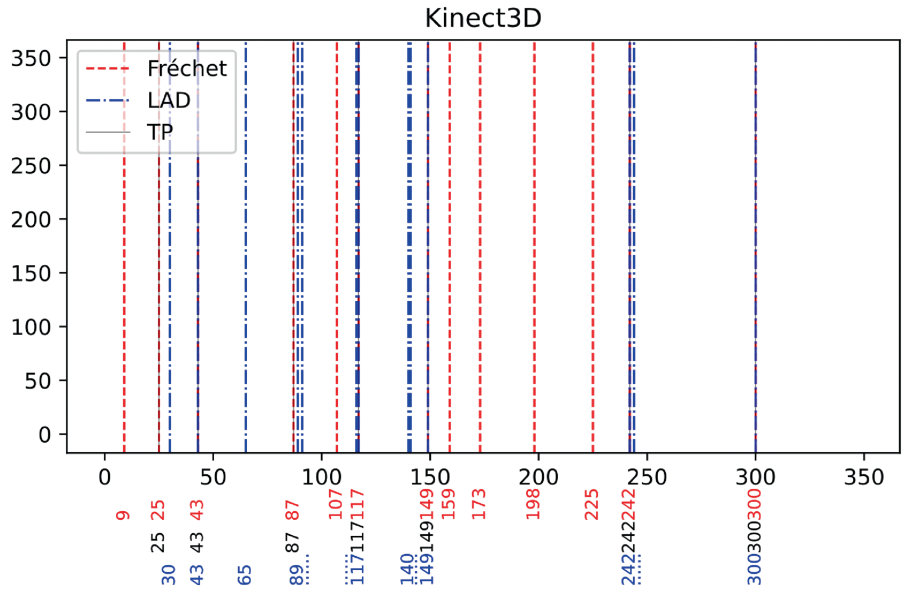

FIGURE 3 | Detection results in the Kinect3D dataset. The figure illustrates change points detected by the Fréchet algorithm, indicated with red dashed lines, alongside those identified by the LAD algorithm, indicated with blue dotted lines. The actual change points are indicated with dark solid lines.

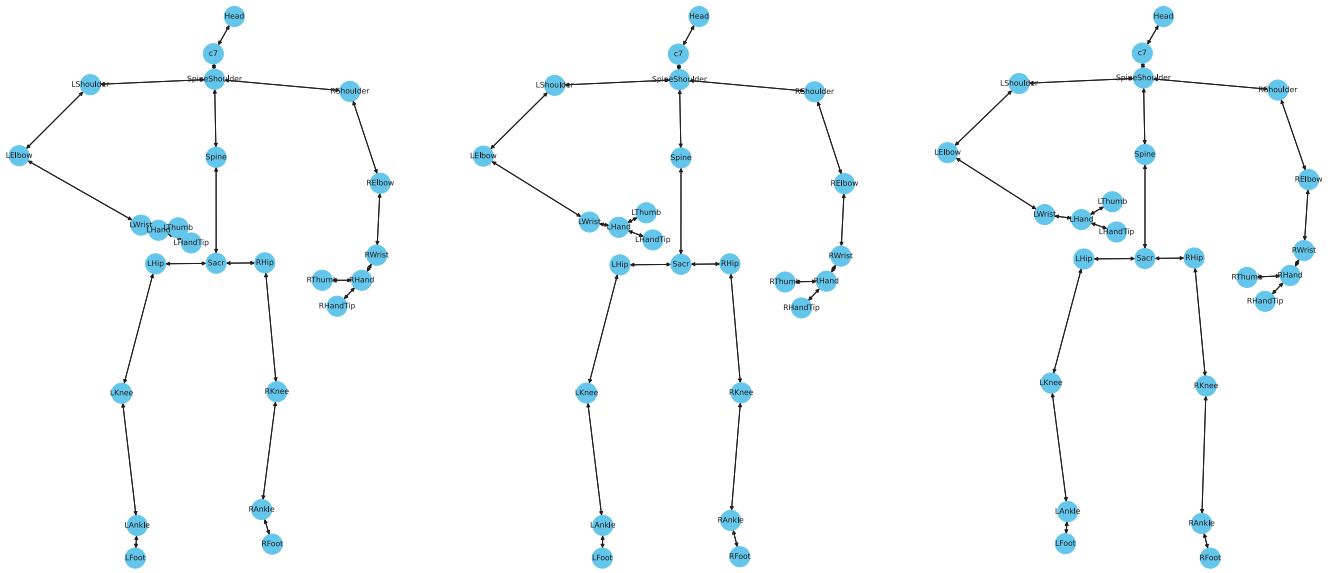

(a) (b) (c)

FIGURE 4 | (a) Sequence at "197" in the Kinect3D dataset. (b) "198". (c) "199".

out of 328 sequences, the dark solid line represents actual change points. The Fréchet algorithm successfully detected all 7 true change points (depicted in red). However, the LAD algorithm missed 2 change points and only detected 5 out of the 7 actual change points. Figure 3 illustrates the change points identified by both our algorithm and the baseline method, with the actual change points highlighted for emphasis.

Upon further inspection of the misjudged points, this study conducted a meticulous frame-by-frame analysis to investigate the underlying reasons for the misclassifications. At position 9, a sudden deformation in the left elbow was observed. Moreover, positions 107, 159, 198, and 225 exhibited an abrupt change in the direction of the left thumb, as illustrated in Figure 4, with subfigures (a), (b), and (c) highlighting the specific instances. Furthermore, at position 173, the ankle displayed a sudden inward turn, potentially increasing the risk of spraining, as depicted in Figure 5, with subfigures (a), (b), and (c) providing visual evidence. Based on these observations, this study hypothesizes that the target subject may experience irregular tremors in the left hand, possibly induced by Parkinson's disease. Additionally,

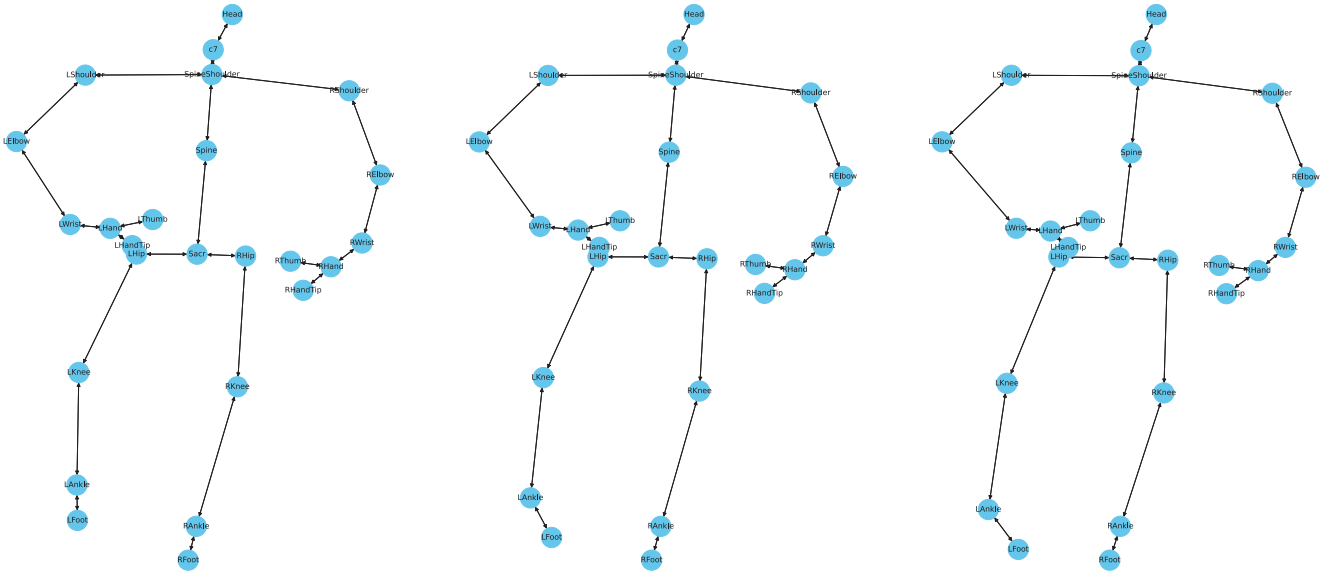

FIGURE 5 | (a) Sequence at "172" in the Kinect3D dataset. (b) "173". (c) "174".

the identification of another potential change point could offer valuable insights for preventing the patient from falling.

To validate the robustness of the algorithm and highlight the advantages of the Log-Euclidean metric, we also conducted experiments using the Euclidean metric (Fréchet-Euclid), the Riemannian metric (Fréchet-Riemann), and a version without computing the nearest positive definite matrix (Fréchet-WithoutPD). In order to investigate whether compressing graphs results in the loss of spatial information regarding the relative positions of joints, we modified the original dataset (25 nodes, 24 edges) to create six variations: removing the thumb and fingertip (21 nodes, 20 edges), detaching the arm (14 nodes, 14 edges), removing the head and jaw (23 nodes, 22 edges), and two versions of external peripheral connections (25 nodes, 36 edges and 25 nodes, 27 edges). These datasets were labeled as Kinect3D1-6. Each experiment was run 1000 times, and we computed the average runtime as well as key accuracy metrics (Precision, Recall, F1-Score). As shown in Tables 1 and 2, Fréchet demonstrates higher accuracy and shorter running times across all datasets compared to other methods.

In addition, we plotted the accuracy and false-positive rate curves (FPR) of LAD on the Kinect3D1-6 dataset using the Fréchet-Euclidean metric, without computing the nearest positive definite matrix (Frechet-WithoutPD), as shown in Figure 6. Our method demonstrates higher accuracy and lower false-positive rates compared to other Fréchet-based metrics. This highlights the robustness and precision of our approach, which leverages the log-Euclidean Fréchet metric, even when certain structural graph information is missing. Furthermore, although compressing images into graphs does indeed result in the loss of some spatial information regarding the relative positions of joints, it can be observed from Figure 6 that our algorithm is capable of recognizing the changes, despite a certain level of false positives. Simultaneously, we have also conducted relevant indicators for the Fréchet algorithm with a confidence window (Fréchet-CW). Our calculation method considers a change point as detectable if it falls within the designated interval. As shown in the table, compared to other methods, Fréchet-CW achieves a lower false positive rate while maintaining high accuracy.

In conclusion, this study found that the Fréchet algorithm, compared to the LAD algorithm, exhibits higher precision in identifying the starting and ending points of gait transitions in Parkinson's patients, making it more suitable for preventing falls and avoiding greater injuries. The limited Kinect3D sample data led to the generation of excess predictions, and future improvements are anticipated in enhancing the data source.

2. AlphaPose

For AlphaPose, the results of multiple change points are displayed in Figure 7. It can be observed that out of 875 sequences, the dark solid line represents actual change points. The Fréchet algorithm successfully detected all true change points except for "482" and "811", which were correctly not identified as change points due to being instances of the same gait. Figure 7 shows the change points identified by both our algorithm and the baseline method, with the actual change points highlighted.

Upon conducting a frame-by-frame analysis similar to the approach employed for the Kinect3D dataset, we investigated the reasons behind the misjudgments in the AlphaPose dataset. The analysis revealed that at positions 208 and 425, the distance between the target object's left ankle and knee underwent a significant reduction. Similarly, at positions 600 and 852, a substantial decrease in the distance between the right ankle and knee was observed. Furthermore, at position 645, a change was detected due to the crossing activity of the forearm. These potential change

TABLE 1 | Comparative performance metrics of the proposed Fréchet algorithms and baseline methods in terms of precision and recall across six datasets after 1000 experimental runs.

Method	LAD		Fréchet-SN		Fréchet-Euclid		Fréchet–Riemann		Fréchet-WithoutPD		Fréchet		Fréchet-CW	
Dataset	Precision	Recall	Precision	Recall	Precision	Recall	Precision	Recall	Precision	Recall	Precision	Recall	Precision	Recall
Kinect3D1	0.3846	0.7143	0.1111	0.8571	0.2500	0.8571	0.1579	0.4286	0.3889	1.0000	0.5385	**1.0000**	**0.6364**	**1.0000**
Kinect3D2	0.3846	0.7143	0.0322	0.2857	0.2500	0.8571	0.0000	0.0000	0.2174	0.7143	0.4000	0.8571	**0.4615**	**0.8571**
Kinect3D3	0.3077	0.5714	0.0303	0.2857	0.3043	1.0000	0.05882	0.1429	0.3333	0.4286	0.2941	0.7143	**0.3846**	0.7143
Kinect3D4	0.3846	0.7143	0.0597	0.5714	0.2500	0.8571	0.0000	0.0000	0.3889	1.0000	0.2917	**1.0000**	**0.4375**	**1.000**
Kinect3D5	0.3846	0.7143	0.0755	0.5714	0.1613	0.7143	0.2258	1.0000	0.2609	0.8571	**0.4000**	0.8571	**0.4000**	0.8571
Kinect3D6	0.3077	0.5714	0.0455	0.4286	0.1579	0.4286	0.2609	0.8571	0.2857	0.8571	0.3158	**0.8571**	**0.4286**	**0.8571**

TABLE 2 | Comparative performance metrics of the proposed Fréchet algorithms and baseline methods in terms of F1-score and Average Runtime (AR) across six datasets after 1000 experimental runs.

Method	LAD		Fréchet-SN		Fréchet-Euclid		Fréchet–Riemann		Fréchet-WithoutPD		Fréchet		Fréchet-CW	
Dataset	F1-score	AR(s)	F1-score	AR(s)	F1-score	AR(s)	F1-score	AR(s)	F1-score	AR(s)	F1-score	AR(s)	F1-score	AR(s)
Kinect3D1	0.5000	1.2194	0.1967	104.1770	0.3870	6.3388	0.2308	6.9867	0.5600	8.5063	0.7000	8.0524	**0.7778**	6.9168
Kinect3D2	0.5000	0.9988	0.0580	76.8202	0.3870	6.4329	0.0000	2.7201	0.3333	8.8443	0.5455	9.0347	**0.6000**	7.7959
Kinect3D3	0.4000	0.8238	0.0548	45.8717	0.4667	5.4595	0.0833	3.7464	0.3750	3.0721	0.4167	5.5890	**0.5000**	4.3694
Kinect3D4	0.5000	1.0816	0.1081	78.6406	0.3870	5.6793	0.0000	2.6661	0.5600	9.0254	0.4516	8.3141	**0.6087**	7.3704
Kinect3D5	0.5000	1.0861	0.1333	89.6348	0.2632	8.4753	0.3684	20.2481	0.4000	10.3753	**0.5455**	9.6624	**0.5454**	7.9738
Kinect3D6	0.4000	1.0781	0.0822	101.5233	0.2308	4.5095	0.4000	11.0991	0.4286	8.5366	0.4615	8.9785	**0.5714**	8.1098

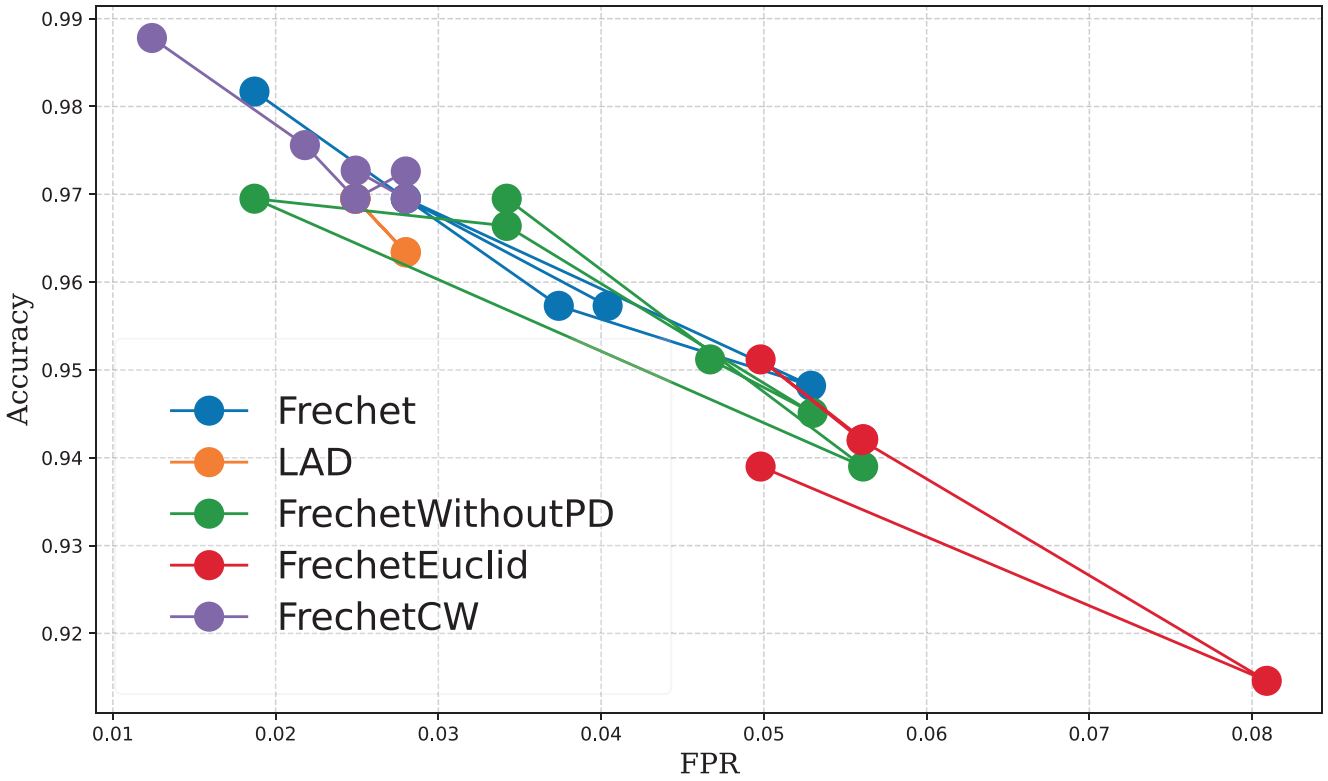

FIGURE 6 | The figure shows the performance of the Fréchet and Fréchet-CW algorithms, along with their comparison methods, on the Kinect3D1-6 dataset. The x-axis represents the false positive rate, and the y-axis represents accuracy. Due to their poor performance, we excluded the Fréchet–Riemann and Fréchet-SN methods from our analysis.

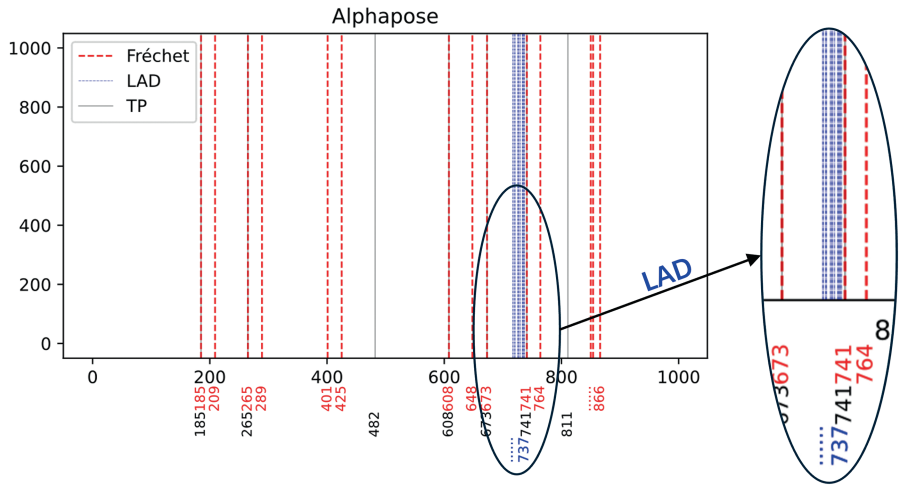

FIGURE 7 | Detection results in the AlphaPose dataset. The figure illustrates change points detected by the Fréchet algorithm, indicated with red dashed lines, alongside those identified by the LAD algorithm, indicated with blue dotted lines. The actual change points are indicated with dark solid lines.

points share a common characteristic: they are all associated with excessive movements resulting from shifts in the body's center of gravity. The identification of these change points provides valuable information for assessing the likelihood of falling and can contribute to the development of preventive measures.

In addition, it is particularly noteworthy that this experiment based on AlphaPose has significantly demonstrated the superiority of the Fréchet algorithm over the LAD algorithm. The study noted that there is a substantial difference between the two algorithms in estimating the location of change points. The blue color represents the LAD algorithm, with its test statistics significantly ranging within [717, 737]. After analyzing the videos generated from the raw data, it can be determined that the reason the LAD algorithm focuses on detecting change points within the [717, 737] interval is due to an evident fall occurring within this interval, as shown in Figures with subfigures as Figure 8a, b.

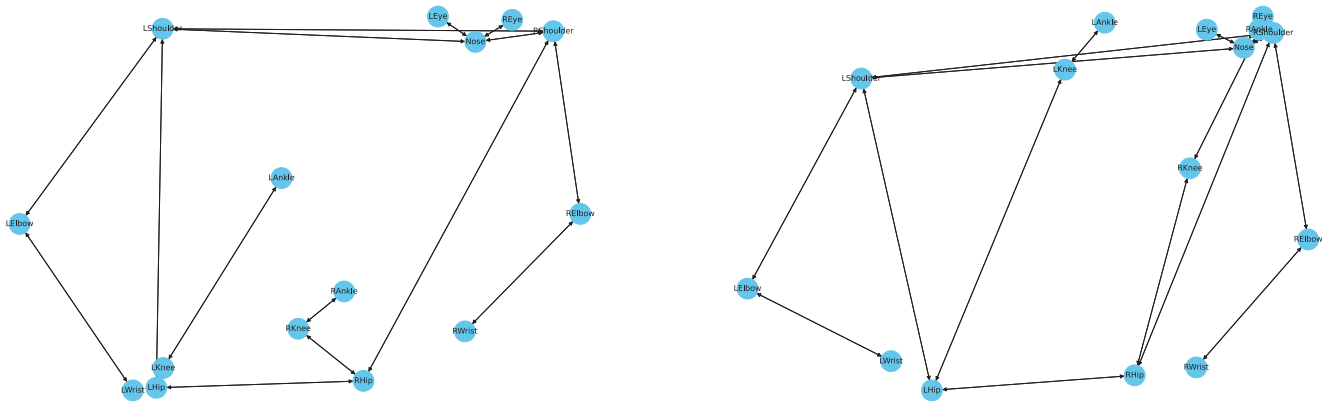

FIGURE 8 | (a) Sequence at "721" in the AlphaPose dataset. (b) "736".

TABLE 3 | After 1000 experimental runs, a comparison of the performance indicators between the proposed Fréchet algorithm and the baseline method across various aspects is conducted on the AlphaPose dataset.

Method	LAD	Fré chet-SN	Fréchet-Euclid	Fréchet–Riemann	Fréchet-WithoutPD	Fréchet	Fréchet-CW
Accuracy	0.9566	0.7977	0.8366	0.7657	0.9897	**0.9897**	0.9828
Precision	0.0571	0.0170	0.0405	0.0286	0.3750	**0.4167**	0.2500
Recall	0.2857	0.4286	0.8571	0.8571	0.4286	0.7143	0.5714
F1-score	0.0952	0.0327	0.0552	0.0774	0.4000	**0.5263**	0.3478
AR(s)	1.1736	133.8507	21.2108	37.1516	4.9329	7.6023	7.2748
FPR	0.0380	0.1993	0.1636	0.2350	0.0057	**0.0080**	0.0138

This signifies that when the LAD detects an obvious change point, the patient has already fallen. The LAD algorithm focuses on the entire fall process, overlooking other gait freezes that could lead to the fall. In other words, it cannot provide a preventive warning function.

In contrast, the Fréchet algorithm-based Parkinson's gait freeze detection method in this study can better focus on the starting and ending points of the gait transitions in Parkinson's patients. From the detection results, it can be seen that the red color represents the Fréchet algorithm, and the black color represents the actual transformation points. The Fréchet algorithm correctly detected the change points at 185, 265, 608, 673, 741, and 811, exhibiting high accuracy. Therefore, it is more suitable for providing early warnings to prevent patient falls, thereby avoiding greater irreversible harm.

We have incorporated two additional metrics: accuracy and false positive rate. As evident from Table 3, our algorithm exhibits superior performance on the AlphaPose dataset when compared to other algorithms. Our approach precisely identifies change points while maintaining an exceptionally low false positive rate. Conversely, other measurement methods either fail to detect change points altogether or exhibit excessively high false positive rates.

In conclusion, through comparison, we discovered that the determination of change points and the exploration of potential change points based on the AlphaPose dataset are more accurate than those based on the Kinect3D dataset. Our results indicate that the AlphaPose dataset can predict 3D joint positions using only standard color video. This eliminates the need for specialized depth cameras such as the Microsoft Kinect while also increasing the distance at which participants' gait can be analyzed. This simplifies the monitoring costs.

5 | Conclusion

In this study, we propose a novel approach for detecting FOG from natural gait videos of PD patients. The approach produces a pose graph sequence that models the patient's posture over time. It offers two key advantages over existing methods. First, it provides a new feature extraction method based on matrices that focuses on the connectivity within the human skeleton, as opposed to relying on pixel data as in deep learning methods. Second, it adopts an SVD approach of graph Laplacian matrices so as to employ the Log-Euclidean metric to derive their Fréchet mean and variance. To validate the effectiveness of our proposed algorithm, we conducted extensive experiments using two real-world datasets. The performance of our method was compared against the LAD baseline method, and the results demonstrate the superior accuracy and reliability of our approach in identifying FOG break points in time.

Looking ahead, there are several promising avenues for future research. First, our algorithm operates on video segments. Incorporating it with more advanced engineering could enable full-duration detection of FOG and lead to practical applications. Second, the extension of our approach to other gait disorders and movement abnormalities could broaden its applicability and impact.

Acknowledgments

This research was supported by the City University of Hong Kong (9610639), the Hong Kong Polytechnic University (ZZQ2), the Hong Kong SAR Government (GRF15301123), the National Natural Science Foundation of China (12301338), and the Chengdu Municipal Office of Philosophy and Social Science (2024BS013).

Conflicts of Interest

The authors declare no conflicts of interest.

Data Availability Statement

The data that supports the findings of this study are available in the Supporting Information of this article.

Endnotes

[1] Weak convergence is a function space generalization of convergence in distribution [36].

References

1. J. Y. Y. Kwok, R. Smith, L. M. L. Chan, et al., "Managing Freezing of Gait in Parkinson's Disease: A Systematic Review and Network Meta-Analysis," *Journal of Neurology* 269, no. 6 (2022): 3310–3324.

2. R. Guo, X. Cheng, Z. C. Hou, et al., "A Shoe-Integrated Sensor System for Long-Term Center of Pressure Evaluation," *IEEE Sensors Journal* 21, no. 23 (2021): 27037–27044.

3. A. Sabo, S. Mehdizadeh, A. Iaboni, and B. Taati, "Estimating Parkinsonism Severity in Natural Gait Videos of Older Adults With Dementia," *IEEE Journal of Biomedical and Health Informatics* 26, no. 5 (2022): 2288–2298.

4. P. Dubey and H. G. Müller, "Fréchet Change-Point Detection," *Annals of Statistics* 48, no. 6 (2020): 3312–3335.

5. N. J. Higham, "Computing the Nearest Correlation Matrix-A Problem From Finance," *IMA Journal of Numerical Analysis* 22, no. 3 (2002): 329–343.

6. V. Arsigny, P. Fillard, X. Pennec, and N. Ayache, "Geometric Means in a Novel Vector Space Structure on Symmetric Positive-Definite Matrices," *SIAM Journal on Matrix Analysis and Applications* 29, no. 1 (2007): 328–347.

7. K. Wirdefeldt, H. O. Adami, P. Cole, D. Trichopoulos, and J. Mandel, "Epidemiology and Etiology of Parkinson's Disease: A Review of the Evidence," *European Journal of Epidemiology* 26 (2011): 1–58.

8. Y. Okuma, "Freezing of Gait in Parkinson's Disease," *Journal of Neurology* 253 (2006): 27–32.

9. T. Ashfaque Mostafa, S. Soltaninejad, T. L. McIsaac, and I. Cheng, "A Comparative Study of Time Frequency Representation Techniques for Freeze of Gait Detection and Prediction," *Sensors* 21, no. 19 (2021): 6446.

10. M. Morris, R. Iansek, T. Matyas, and J. Summers, "Abnormalities in the Stride Length-Cadence Relation in Parkinsonian Gait," *Movement Disorders: Official Journal of the Movement Disorder Society* 13, no. 1 (1998): 61–69.

11. S. Lahmiri, "Gait Nonlinear Patterns Related to Parkinson's Disease and Age," *IEEE Transactions on Instrumentation and Measurement* 68, no. 7 (2018): 2545–2551.

12. D. Urso, V. Leta, L. Batzu, et al., "Disentangling the PIGD Classification for the Prediction of Cognitive Impairment in De Novo Parkinson's Disease," *Journal of Neurology* 269, no. 3 (2022): 1566–1573.

13. A. Taweekitikul, P. Tanvijit, P. Tantisuvanitchkul, et al., "Validity and Reliability of the Thai Version of the Freezing of Gait Questionnaire in Individuals With parkinson's Disease," *Annals of Rehabilitation Medicine* 47, no. 1 (2023): 45–51.

14. M. Lu, Q. Zhao, K. L. Poston, et al., "Quantifying Parkinson's Disease Motor Severity Under Uncertainty Using MDS-UPDRS Videos," *Medical Image Analysis* 73 (2021): 102179.

15. G. Prateek, I. Skog, M. E. McNeely, R. P. Duncan, G. M. Earhart, and A. Nehorai, "Modeling, Detecting, and Tracking Freezing of Gait in Parkinson Disease Using Inertial Sensors," *IEEE Transactions on Biomedical Engineering* 65, no. 10 (2017): 2152–2161.

16. W. Zhang, Z. Yang, H. Li, et al., "Multimodal Data for the Detection of Freezing of Gait in Parkinson's Disease," *Scientific Data* 9, no. 1 (2022): 606.

17. Y. Hou, J. Ji, Y. Zhu, T. Dell, and X. Liu, "Flexible Gel-Free Multi-Modal Wireless Sensors With Edge Deep Learning for Detecting and Alerting Freezing of Gait Symptom," *IEEE Transactions on Biomedical Circuits and Systems* 17, no. 5 (2023): 1010–1021.

18. E. E. Asher, M. Plotnik, M. Günther, et al., "Connectivity of EEG Synchronization Networks Increases for Parkinson's Disease Patients With Freezing of Gait," *Communications Biology* 4, no. 1 (2021): 1017.

19. A. Pfister, A. M. West, S. Bronner, and J. A. Noah, "Comparative Abilities of Microsoft Kinect and Vicon 3D Motion Capture for Gait Analysis," *Journal of Medical Engineering & Technology* 38, no. 5 (2014): 274–280.

20. B. Müller, W. Ilg, M. A. Giese, and N. Ludolph, "Validation of Enhanced Kinect Sensor Based Motion Capturing for Gait Assessment," *PLoS One* 12, no. 4 (2017): e0175813.

21. K. Sato, Y. Nagashima, T. Mano, A. Iwata, and T. Toda, "Quantifying Normal and Parkinsonian Gait Features From Home Movies: Practical Application of a Deep Learning–Based 2D Pose Estimator," *PLoS One* 14, no. 11 (2019): e0223549.

22. M. H. Li, T. A. Mestre, S. H. Fox, and B. Taati, "Vision-Based Assessment of Parkinsonism and Levodopa-Induced Dyskinesia With Pose Estimation," *Journal of Neuroengineering and Rehabilitation* 15 (2018): 1–13.

23. T. Nguyen Nguyen, H. H. Huynh, and J. Meunier, "Estimating Skeleton-Based Gait Abnormality Index by Sparse Deep Auto-Encoder," 2019, *arXiv e-prints*.

24. K. Jun, D. W. Lee, K. Lee, S. Lee, and M. S. Kim, "Feature Extraction Using an RNN Autoencoder for Skeleton-Based Abnormal Gait Recognition," *IEEE Access* 8 (2020): 19196–19207.

25. H. Tian, H. Li, W. Jiang, et al., "Cross-Spatiotemporal Graph Convolution Networks for Skeleton-Based Parkinsonian Gait MDS-UPDRS Score Estimation," *IEEE Transactions on Neural Systems and Rehabilitation Engineering* 32 (2024): 412–421.

26. M. H. Li, T. A. Mestre, S. H. Fox, and B. Taati, "Automated Vision-Based Analysis of Levodopa-Induced Dyskinesia With Deep Learning," in *39th Annual International Conference of the IEEE Engineering in Medicine and Biology Society*, vol. 2017 (IEEE, 2017), 3377–3380.

27. K. Hu, Z. Wang, S. Mei, et al., "Vision-Based Freezing of Gait Detection With Anatomic Directed Graph Representation," *IEEE Journal of Biomedical and Health Informatics* 24, no. 4 (2019): 1215–1225.

28. R. Guo, X. Shao, C. Zhang, and X. Qian, "Sparse Adaptive Graph Convolutional Network for Leg Agility Assessment in Parkinsos Disease,"

IEEE Transactions on Neural Systems and Rehabilitation Engineering 28, no. 12 (2020): 2837–2848.

29. V. Arsigny, P. Fillard, X. Pennec, and N. Ayache, "Log-Euclidean Metrics for Fast and Simple Calculus on Diffusion Tensors," *Magnetic Resonance in Medicine: An Official Journal of the International Society for Magnetic Resonance in Medicine* 56, no. 2 (2006): 411–421.

30. Z. Lin, "Riemannian Geometry of Symmetric Positive Definite Matrices via Cholesky Decomposition," *SIAM Journal on Matrix Analysis and Applications* 40, no. 4 (2019): 1353–1370.

31. C. E. Ginestet, J. Li, P. Balachandran, S. Rosenberg, and E. D. Kolaczyk, "Hypothesis Testing for Network Data in Functional Neuroimaging," *Annals of Applied Statistics* 11 (2017): 725–750.

32. P. R. Halmos, "Positive Approximants of Operators," *Indiana University Mathematics Journal* 21, no. 10 (1972): 951–960.

33. N. Bourbaki, *Lie Groups and Lie Algebras: Chapters*, vol. 7 (Springer-Verlag, 2008).

34. A. Petersen and H. G. Müller, "Fréchet Regression for Random Objects With Euclidean Predictors," *Annals of Statistics* 47, no. 2 (2019): 691–719.

35. P. Dubey and H. G. Müller, "Fréchet Analysis of Variance for Random Objects," *Biometrika* 106, no. 4 (2019): 803–821.

36. P. Billingsley, *Convergence of Probability Measures* (John Wiley & Sons, 2013).

37. J. Wellner, *Weak Convergence and Empirical Processes: With Applications to Statistics* (Springer Science & Business Media, 2013).

38. Y. Thanwerdas and X. Pennec, "The Geometry of Mixed-Euclidean Metrics on Symmetric Positive Definite Matrices," *Differential Geometry and its Applications* 81 (2022): 101867.

39. K. T. Sturm, "Probability Measures on Metric Spaces of Nonpositive," *Heat Kernels and Analysis on Manifolds, Graphs, and Metric Spaces* 338 (2003): 357.

40. K. T. Sturm, "On the Geometry of Metric Measure Spaces," *Acta Mathematica* 196 (2006): 65–121.

41. A. Guntuboyina and B. Sen, "Covering Numbers for Convex Functions," *IEEE Transactions on Information Theory* 59, no. 4 (2012): 1957–1965.

42. H. Cho and P. Fryzlewicz, "Multiscale and Multilevel Technique for Consistent Segmentation of Nonstationary Time Series," *Statistica Sinica* 42 (2012): 207–229.

43. S. Huang, Y. Hitti, G. Rabusseau, and R. Rabbany, "Laplacian Change Point Detection for Dynamic Graphs," in *Proceedings of the 26th ACM SIGKDD International Conference on Knowledge Discovery & Data Mining* (Association for Computing Machinery, 2020), 349–358.

44. M. R. Gahrooei and K. Paynabar, "Change Detection in a Dynamic Stream of Attributed Networks," *Journal of Quality Technology* 50, no. 4 (2018): 418–430.

45. L. Akoglu and C. Faloutsos, "Event Detection in Time Series of Mobile Communication Graphs," in *Army Science Conference* (2010).

46. S. Ranshous, S. Shen, D. Koutra, S. Harenberg, C. Faloutsos, and N. F. Samatova, "Anomaly Detection in Dynamic Networks: A Survey," *Wiley Interdisciplinary Reviews: Computational Statistics* 7, no. 3 (2015): 223–247.

47. F. Jiang, C. Zhu, and X. Shao, "Two-Sample and Change-Point Inference for Non-Euclidean Valued Time Series," *Electronic Journal of Statistics* 18, no. 1 (2024): 848–894.

48. S. Mehdizadeh, E. Dolatabadi, K. D. Ng, et al., "Vision-Based Assessment of Gait Features Associated With Falls in People With Dementia," *Journals of Gerontology: Series A* 75, no. 6 (2019): 1148–1153.

49. E. Dolatabadi, B. Taati, and A. Mihailidis, "Concurrent Validity of the Microsoft Kinect for Windows v2 for Measuring Spatiotemporal Gait Parameters," *Medical Engineering & Physics* 38, no. 9 (2016): 952–958.

50. P. Yushkevich, Y. Gao, and G. Gerig, *2016 38th Annual International Conference of the IEEE Engineering in Medicine and Biology Society* (IEEE, 2016).

51. S. Mehdizadeh, A. Sabo, K. D. Ng, et al., "Predicting Short-Term Risk of Falls in a High-Risk Group With Dementia," *Journal of the American Medical Directors Association* 22, no. 3 (2021): 689–695.

52. R. Huitema, A. Hof, and K. Postema, "Ultrasonic Motion Analysis System-Measurement of Temporal and Spatial Gait Parameters," *Journal of Biomechanics* 35, no. 6 (2002): 837–842.

53. K. D. Ng, S. Mehdizadeh, A. Iaboni, A. Mansfield, A. Flint, and B. Taati, "Measuring Gait Variables Using Computer Vision to Assess Mobility and Fall Risk in Older Adults With Dementia," *IEEE Journal of Translational Engineering in Health and Medicine* 8 (2020): 1–9.

Supporting Information

Additional supporting information can be found online in the Supporting Information section.

Appendix A

Theoretical Framework

A.1 Proof

Theorem. (**Consistency of Change-Point Estimation**). *Under the alternative hypothesis* H_1 *and assumptions* $(A1)$–$(A3)$, *the estimated change-point* $\hat{\tau}$ *satisfies*

$$\sup_{u\in I_c}|T_n(u)-T(u)| = o_P(1) \quad \textit{and} \quad |\hat{\tau}-\tau| = o_P(1) \quad \textit{as} \quad n\to\infty$$

Proof. The proof utilizes properties of the Log-Euclidean metric space of SPD matrices derived from graph Laplacians.

Step 1: Uniform Convergence of Fréchet Means

Under H_1, we partition the sequence into two segments with distributions P_1 and P_2. By the properties of $(\tilde{\mathcal{L}}, \delta_{LE})$:

- The sample Fréchet means $\overline{X}[0,u]$ and $\overline{X}[u,1]$ exist uniquely and have the closed form:

$$\overline{X}[0,u] = \exp\left(\frac{1}{[nu]}\sum_{i=1}^{[nu]}\log(\tilde{L}^{(i)})\right)$$

- They converge uniformly in probability to their population counterparts μ_1 and μ_2.

Step 2: Convergence of Fréchet Variances

The sample Fréchet variances converge to their population counterparts:

$$s^2_{[0,u]} \xrightarrow{P} \sigma_1^2 \text{ and } s^2_{[u,1]} \xrightarrow{P} \sigma_2^2$$

Step 3: Consistency of $\hat{\tau}$

The controlled metric entropy of $(\tilde{\mathcal{L}}, \delta_{LE})$ and the uniqueness of Fréchet means ensure:

- $T_n(u)$ converges uniformly to a deterministic function $T(u)$.
- $T(u)$ is uniquely maximized at τ.

Therefore, $|\hat{\tau} - \tau| = o_P(1)$. □

Theorem 4. (**Consistency of the Test**). *Under* H_1 *and assumptions* $(A1)$–$(A3)$, *for contiguous alternatives where*

$$\delta_{LE}(\mu_1, \mu_2) = a_n \quad \text{and} \quad |\sigma_1^2 - \sigma_2^2| = b_n$$

with $a_n, b_n \to 0$ *as* $n \to \infty$, *the test power satisfies* $\psi_n \to 1$, *provided either* $\sqrt{n}a_n \to \infty$ *or* $\sqrt{n}b_n \to \infty$.

Proof. **Step 1: Metric Properties**

In $(\tilde{\mathcal{L}}, \delta_{LE})$:

$$\delta_{LE}^2(\overline{X}[0,u], \overline{X}[u,1]) \geq \zeta \delta_{LE}^2(\mu_1, \mu_2)$$

Step 2: Test Statistic Scaling

The test statistic satisfies:

$$nT_n(\tau) \geq \min\{na_n^2, nb_n^2\} \cdot C \quad \textit{for some constant} \quad C > 0$$

Step 3: Power Analysis

Under the scaling conditions:

$$P(\sup_{u \in \tilde{I}_c} n\, T_n(u) > q_{1-\alpha}) \to 1$$

Therefore, $\psi_n \to 1$. □

For detailed proofs, we refer readers to Dubey et al. [4], as our proofs follow the same arguments with the Log-Euclidean metric specific to our setting.